OPEN ACCESS



AWSoM Magnetohydrodynamic Simulation of a Solar Active Region with Realistic Spectral Synthesis

Tong Shi¹, Ward Manchester IV¹, Enrico Landi¹, Bart van der Holst¹, Judit Szente¹, Yuxi Chen¹, Gábor Tóth¹, Luca Bertello², and Alexander Pevtsov²

Department of Climate and Space Sciences and Engineering, University of Michigan, Ann Arbor, MI 48109, USA National Solar Observatory, 3665 Discovery Drive, 3rd Floor, Boulder, CO 80303, USA Received 2021 October 2; revised 2022 January 31; accepted 2022 February 6; published 2022 March 24

Abstract

For the first time, we simulate the detailed spectral line emission from a solar active region (AR) with the Alfvén Wave Solar Model (AWSoM). We select an AR appearing near disk center on 2018 July 13 and use the National Solar Observatory's Helioseismic and Magnetic Imager synoptic magnetogram to specify the magnetic field at the model's inner boundary. To resolve small-scale magnetic features, we apply adaptive mesh refinement with a horizontal spatial resolution of 0°.35 (4.5 Mm), four times higher than the background corona. We then apply the SPECTRUM code, using CHIANTI spectral emissivities, to calculate spectral lines forming at temperatures ranging from 0.5 to 3 MK. Comparisons are made between the simulated line intensities and those observed by Hinode/Extreme-ultraviolet Imaging Spectrometer where we find close agreement across a wide range of loop sizes and temperatures (about 20% relative error for both the loop top and footpoints at a temperature of about 1.5 MK). We also simulate and compare Doppler velocities and find that simulated flow patterns are of comparable magnitude to what is observed. Our results demonstrate the broad applicability of the low-frequency AWSoM for explaining the heating of coronal loops.

Unified Astronomy Thesaurus concepts: Solar corona (1483); Spectrophotometry (1556); Magnetohydrodynamics (1964); Magnetohydrodynamical simulations (1966); Solar coronal waves (1995)

1. Introduction

The coronal heating problem has been a major challenge in solar physics, and a tremendous amount of efforts have been made over the past several decades (Kuperus et al. 1981; Zirker 1993; Gudiksen & Nordlund 2005; Ofman 2005b; Klimchuk 2006; Taroyan & Erdélyi 2009; Mathioudakis et al. 2013; Aschwanden 2019; Van Doorsselaere et al. 2020). The convective motions in and below the solar photosphere provide abundant energy for the hot corona. The question is how this energy is transferred and released into the corona above, heats up the plasma, and accelerates the solar wind.

Based on the convective timescales, as compared to the Alfvén transit time in the corona, two main classes of heating mechanisms are most promising. Slow/quasi-static stressing causes twisting and braiding of the field and results in magnetic reconnections and energy release in current sheets, which is also known as direct current heating (Parker 1988; Priest & Schrijver 1999; Fujimoto et al. 2011). Fast motions generate magnetohydrodynamics (MHD) waves, and the wave dissipation is also known as alternating current (AC) heating (Alfvén 1947; Osterbrock 1961; Ionson 1978). Growing evidence shows that the two mechanisms interact with each other (e.g., dissipation of current sheets involves waves, and waves can drive reconnection), and MHD turbulence and small-scale reconnections are also linked (Mathioudakis et al. 2013; De Moortel & Browning 2015; Velli et al. 2015; Aschwanden 2019). The interesting question then is which of these processes is the dominant energy source at different locations and/or times.

Original content from this work may be used under the terms of the Creative Commons Attribution 4.0 licence. Any further distribution of this work must maintain attribution to the author(s) and the title of the work, journal citation and DOI.

Currently, limited by computing capabilities on one side and telescope sensitivity and temporal and spatial resolution on the other, it is very difficult to properly explain the coronal heating problem for observers, theorists, and modelers, let alone tackling the complex coupling between the dense solar interior and the tenuous outer atmosphere spanning over multiple orders of magnitude (Parnell & De Moortel 2012). In addition, the problem of coronal heating is intrinsically linked to that of solar wind acceleration, as both reconnection and wave dissipation mechanisms are also good candidates for solar wind acceleration (Cranmer 2009).

Among the class of AC-heating mechanisms, Alfvén wave turbulent heating models have recently gained much attention (e.g., Tu & Marsch 1995; Cranmer 2009; Van Doorsselaere et al. 2020). Pioneering work of Coleman (1968) showed the importance of turbulence in solar wind with Mariner 2 measurements near 1 au, while the high correlation of velocity and magnetic field fluctuations as measured by Belcher & Davis (1971) opened up new questions about the nature of such solar wind fluctuations (Tu & Marsch 1995). Inspired by the fluctuation spectrum slope that follows the Kolmogorov power law (Bayassano et al. 1982; Denskat & Neubauer 1982; Denskat et al. 1983), Tu et al. (1984) developed a WKB-like turbulence model taking into account the turbulent energy cascade effects. Many other successful early models include Ofman & Davila (1998), Ofman (2005a), Bogdan et al. (2002), Bogdan et al. (2003), Usmanov et al. (2000), Hu et al. (2003). Suzuki & Inutsuka (2005, 2006) performed a first self-consistent onedimensional (1D) MHD simulation of solar wind heating and acceleration driven by the dissipation of low-frequency Alfvén waves, through the generation of the compressive waves and shocks. The model was further developed into 2D by Matsumoto & Suzuki (2012) taking into account the turbulent cascade.

Cranmer et al. (2007) obtained realistic slow and fast solar wind conditions and reproduced in situ ion charge states with their self-consistent 1D turbulence-driven coronal heating model using a phenomenological cascade rate (Zhou & Matthaeus 1990; Hossain et al. 1995; Matthaeus et al. 1999; Dmitruk et al. 2001, 2002). To fully understand the heating in loops, van Ballegooijen et al. (2011) developed a time-dependent 3D reduced MHD turbulence model and were able to reproduce the observed rates of chromospheric and coronal heating in the active region (AR). The nonlinear interactions between the outward and inward propagating waves were realized to be important (Dobrowolny et al. 1980; Velli et al. 1989), and balanced (having equal power for the oppositely propagating waves) and imbalanced cascades had been extensively studied (Goldreich & Sridhar 1995; Ng & Bhattacharjee 1996; Goldreich & Sridhar 1997; Galtier et al. 2000; Lithwick & Goldreich 2003: Lithwick et al. 2007). Some of the other recent 3D turbulent heating models include Perez & Chandran (2013), van der Holst et al. (2014), Downs et al. (2016), van Ballegooijen et al. (2017), van Ballegooijen & Asgari-Targhi (2018), Chandran & Perez (2019).

Our Alfvén Wave Solar Model (AWSoM; van der Holst et al. 2010; Sokolov et al. 2013; van der Holst et al. 2014; Meng et al. 2015) is a 3D data-driven MHD model that can run either standalone or as a component of the Space Weather Modeling Framework (SWMF; Tóth et al. 2005, 2012). AWSoM models a self-consistent Alfvén wave turbulencedriven solar corona (SC), starting from the upper chromosphere, through the transition region, to the corona, and finally into the inner-heliosphere (IH) up to 1 au and even beyond. It aims at reproducing realistic line-of-sight (LOS) extremeultraviolet (EUV) images as well as 1 au in situ solar wind measurements with a single validated model. AWSoM does not rely on ad hoc heating functions, but instead uses a physicsbased description of the turbulent cascade and dissipative heating from the nonlinear interactions between the oppositely propagating Alfvén waves (Velli et al. 1989; Zank et al. 1996; Matthaeus et al. 1999; Chandran et al. 2011; Zank et al. 2012). Wave reflection and heat partitioning between the electrons and anisotropic protons are also treated self-consistently. Several validation studies have been done and results from AWSoM compare favorably with the observations for both EUV images and in situ measurements (Manchester et al. 2012; Jin et al. 2013; Oran et al. 2013, 2015, 2017; Sachdeva et al. 2019). van der Holst et al. (2019) used AWSoM to predict that the Parker Solar Probe was in close proximity to the heliospheric current sheet and in the slow wind, and also provided several plasma quantities from the model that turned out to be comparable to the actual observation (Riley et al. 2019).

Here, we perform the first validation study with the AWSoM model on ARs with two challenges in mind: (1) it is computationally difficult to simulate an AR at high resolution starting from the upper chromosphere within a global model, rather than in a more limited spatial domain; and (2) we need to simulate spectrally resolved observables that allow a more thorough testing of the Alfvén wave turbulence scenario. In fact, the LOS synthetic images in narrowband channels of the Solar Dynamics Observatory (SDO; Pesnell et al. 2012)/Atmospheric Imaging Assembly (AIA; Boerner et al. 2012; Lemen et al. 2012) commonly used to test models provide information too vague to conduct detailed comparisons. In this work, as the first paper of a series of validations and analysis of

the AWSoM model on an AR, we perform a high-resolution simulation with extra adaptive mesh refinement (AMR) levels for the AR, together with the recently implemented fifth-order numerical scheme with MP5 limiter (Suresh & Huynh 1997; Chen et al. 2016) to further improve accuracy. We use the newly developed SPECTRUM code (Szente et al. 2019) to realistically synthesize the spectral lines, which are optically thin and only sensitive to a very narrow range of temperatures for the densest plasmas, and compare with the high-resolution Hinode (Kosugi et al. 2007)/Extreme Ultraviolet Imaging Spectrometer (EIS; Culhane et al. 2007) observations.

This paper is structured as follows: Section 2 introduces the AWSoM model, the model parameter setup, and the observational data that we use. Section 3 examines our simulation results and does the detailed model-observation comparison on spectral line intensities, Doppler speeds, and line broadening. Section 4 concludes the work and discusses further implications.

2. Data and Model

2.1. Brief Description of the AWSoM Model

We use the AWSoM model for the SC component of the SWMF. The model utilizes the Block Adaptive Tree Solarwind Roe Upwind Scheme (BATSRUS; Powell et al. 1999; Gombosi et al. 2004) to solve the MHD equations in the Heliographic Rotating frame (HGR). The computing domain starts from the lower transition region, and up to 24 solar radii (Rs). The AWSoM model includes the electron temperature, as well as the anisotropic proton temperatures (parallel and perpendicular to the magnetic field) to better account for the heating differences between different directions. In this study, because we mainly focus on an AR in the very low corona, where collisions are abundant, for simplicity, we only use a two-temperature model with electron and isotropic proton temperatures (T_e and T_p , respectively).

The AWSoM model features Alfvén wave turbulence to realistically produce plasma conditions from the low corona to the far-reaching solar wind, which are observed by remote sensing and in situ instruments. On the boundary at the solar surface (inner boundary), the outgoing wave energy density is empirically set by prescribing its Poynting flux, while the returning wave is completely absorbed. Counter-propagating waves are generated on both closed and open fields by partial wave reflections due to the Alfvén wave velocity gradient and vorticity along the field lines (Heinemann & Olbert 1980; Leroy 1980; Velli et al. 1989; Matthaeus et al. 1999; Dmitruk et al. 2002; Verdini & Velli 2007). Nonlinear interactions between the oppositely propagating waves result in turbulent cascade and wave energy dissipation, physically providing coronal heating without the need of ad hoc heating functions. To apportion the total heating to electron and proton temperatures, AWSoM uses physics-based theories of linear wave damping and nonlinear stochastic heating (Chandran et al. 2011). A recently improved version of the code uses cascade rates present in Lithwick et al. (2007), and details can be found in van der Holst et al. (2022). Electron heat conduction for both the collisional and collisionless regimes are also included. Optically thin radiative heat loss in the lower corona is calculated with the radiative cooling curves taken from the CHIANTI database (Dere et al. 1997; Del Zanna et al. 2021).

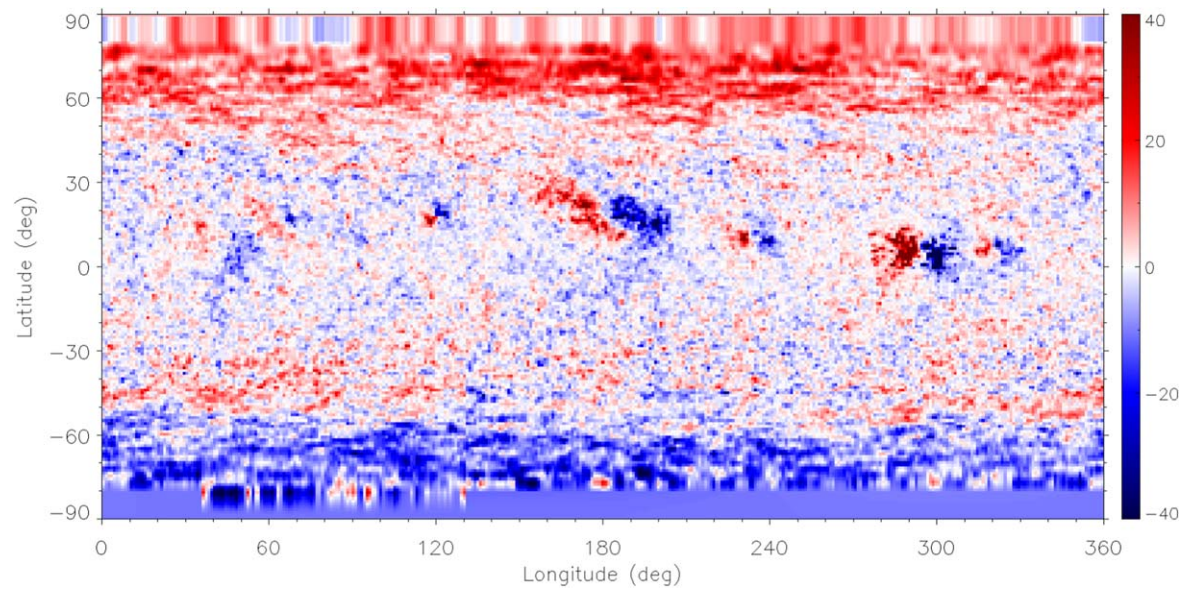


Figure 1. NSO/HMI synoptic map for CR 2206. The AR we study (at about 300° longitude) is patched with SDO/HMI magnetogram at 2018 July 13 13:24. Radial component of the magnetic field is color contoured and in unit [Gauss].

By using the photospheric magnetic field observation as the inner boundary, our model is able to self-consistently develop and heat coronal structures with only a handful of free parameters (density, temperature, and Poynting flux of the Alfvén waves at the boundary; transverse correlation length for the turbulence and heat partitioning; the stochastic heating exponent and amplitude; and two parameters for the collisionless heat conduction, which are only applicable at a distance beyond 10 Rs). The recommended parameter value ranges are chosen empirically with historical observations and optimized according to the model test results. Interested readers may refer to Sokolov et al. (2013), van der Holst et al. (2014), Sachdeva et al. (2019) for more details.

2.2. Data Selection

The AR we selected for this study is an AR with relatively weak average magnetic fields and a simple magnetic structure. It was identified as NOAA AR 12713 during Carrington rotation (CR) 2205 but was too weak to be identified as an AR by NOAA during CR2206 when we examined it. During CR 2206, it was identified as Helioseismic and Magnetic Imager (HMI; Scherrer et al. 2012; Schou et al. 2012) Active Region Patch (HARP; Turmon et al. 2014) 7283. The time we use is 2018-07-13 13:24:00 when this AR is almost at the disk center, so that the projection effect on the magnetogram is the smallest. Since this AR is dispersed and weakened over the rotation, the coronal magnetic field structures are relatively simple and can be well represented by a potential field. There were also no flares or significant activities around the time of study. Thus, it is ideal to be studied without temporal driving with our AWSoM model.

The AR was also well observed by Hinode/EIS with data covering plenty of strong spectral lines. At the time of observation, EIS used the 2'' slit with normal scanning mode (EIS study #544). The field of view (FOV) is $491'' \times 512''$, fully covering the AR. The total time used for the scan is about an hour. We identify the strong spectral lines of interest and then process and fit the EIS data with the standard Solar

Software (SSW) routines. Unfortunately, the default correction (Kamio et al. 2010) for the wavelength drift along the scan direction (caused by the orbital drift of the spacecraft) does not provide a correct Dopplergram for our data. We recalibrated the wavelength offset directly using our data set by assuming that the Doppler shift for the quiet region for all the spectral lines is on average zero (see Peter Young, 2021; EIS Software, Note 16).

An important input for the model is the magnetic map used to specify the field at the inner boundary. We use a synoptic map for CR 2206, produced by the National Solar Observatory (NSO) from SDO/HMI magnetograms (hereafter abbreviated as NSO/HMI; Hughes et al. 2016). Instead of a pseudo-radial magnetic field (obtained by dividing the LOS field by cosine latitude), the NSO/HMI map uses the inverted and fully disambiguated vector magnetograms (Hoeksema et al. 2014) for the full disk data and constructs a vector synoptic map with cosine weights toward the central meridian, which gives the true radial magnetic field component with excellent signal-tonoise. In practice, for our AWSoM code, NSO/HMI synoptic maps usually provide good simulation results during the solar maximum and for studies focused on ARs (see Section 4 for more discussion about the magnetogram products).

We patch the AR in the synoptic map with the cutout from the SDO/HMI full disk data at the time of the study (2018 July 13 13:24) to better avoid the asynchronous nature of the synoptic map. Instead of using the LOS component to estimate the radial magnetic field, we use the SDO/HMI full disk disambiguated vector magnetogram to overcome the projection effect and calculate the radial component. The patch is 70° in longitude and 53° in latitude and is large enough to cover the entire AR. To prevent jumps in the magnetic field at the edges of the patch, a smooth transition with a cosine function is used to stitch the AR patch onto the synoptic map. The resulting merged synoptic map has a 1° resolution in both the longitudinal and latitudinal directions. See Figure 1 for the final product of the map we use as the input for the simulation.

2.3. Model Setup

We perform the solar coronal simulation with the AWSoM model. It uses an adaptive 3D spherical grid in HGR system covering radial distances between 1.001 solar radii (Rs) to 24 Rs. The base resolution is 2°.8 (as viewed from the solar center) in both the longitudinal and latitudinal directions (horizontal directions). We also stretch the grid in the radial direction with the higher resolution near the solar surface. To better resolve the transition region and lower corona, a onelevel-higher AMR is used below 1.7 Rs, giving a base radial resolution near the solar surface of about 4×10^{-4} Rs (295 km). Two more levels of AMRs are used for the AR, resulting in a horizontal resolution of 0°.35 (about 4.5 Mm on the solar surface or 6'' as viewed from the Earth), and a radial resolution of about 10^{-4} Rs (74 km) close to the solar surface and 10^{-3} Rs (722 km) at 1.05 Rs. The total number of cells in our simulation is about 16 million. Despite our best effort in increasing the resolution within computational constraints, it is still very difficult to resolve the fine solar structures. As a comparison, the native pixel size of the SDO/HMI magnetogram is $0^{\circ}.03$ in the horizontal direction, more than 10 times finer than our grid size. Therefore, for the lower corona below 1.7 Rs, we also utilize the newly improved fifth-order scheme with MP5 limiter for the BATSRUS solver (Suresh & Huynh 1997; Chen et al. 2016). In practice, the roughly estimated effect of the fifth-order scheme is about equal to 4 times the resolution improvement than using our regular second-order scheme. Therefore, with the combination of $0^{\circ}.35$ horizontal grid resolution and fifth-order scheme, we estimate the achieved resolution to be about 0° .1 (or 1".7 as viewed from the Earth), which is sufficient to resolve the 1° input synoptic map. This estimated final spatial resolution is the best we have ever achieved with our 3D global AWSoM model, and is even approaching SDO/AIA and Hinode/EIS pixel sizes (0".6 and 1", respectively).

The initial and inner boundary (at 1.001 Rs) conditions for the magnetic field are based on the (AR patched) synoptic map. We first calculate a 3D potential magnetic field solution corresponding to the synoptic map with the Finite Difference Iterative Potential-field Solver (FDIPS; Tóth et al. 2011) where the source surface (where the magnetic field becomes purely radial) is located at 2.5 Rs. The FDIPS code provides a solution that exactly matches the radial magnetic field component at the inner boundary, while not being affected by the Gibbs phenomenon that the harmonics method may have. This potential field is then set as the initial condition for the simulation. At the inner boundary, the radial magnetic field component is fixed to be this FDIPS solution, while the horizontal components are allowed to adjust freely.

In order to resolve the extremely steep radial gradients produced by heat conduction and radiation, we artificially broaden the transition region and push the corona outward to overcome the numerical restrictions on radial resolution (Lionello et al. 2009; Sokolov et al. 2013). At the inner boundary, the density is set to be $N_e = 2 \times 10^{11}$ cm⁻³ with a temperature of $T_e = T_p = 5 \times 10^4$ K. This density is overestimated to suppress potential chromospheric evaporation that may become excessive, and allow the upper transition region and corona to reach the correct density. In practice, the density rapidly falls through the lower transition region, and the coronal solution above about 1.03 Rs is not affected (Lionello et al. 2009; van der Holst et al. 2014; Sachdeva et al. 2019).

The initial density, temperature, and velocity in the domain are set to be reasonable values but do not affect the final solution, as they are allowed to fully relax before any meaningful analysis is conducted. The Poynting flux for the Alfvén wave energy density is chosen to be $(S_A/|B|) = 0.5 \times 10^6$ W m⁻² T⁻¹, where S_A is the Poynting flux and |B| is the magnetic field strength at the solar surface. Empirically, this parameter produces results that best compare with observations when set in a range from 0.3 to 1.1 MW m⁻² T⁻¹ (Sachdeva et al. 2021). All the other parameters are set as the default empirical values, and the reader may refer to Sachdeva et al. (2019) for details. Also keep in mind that these empirical values (and recommended value ranges) for AWSoM are chosen according to historical observations and to optimize the 1 au solar wind comparisons.

The simulation is first run in the second-order solver with progressively increasing levels of AMR for 100,000 iterations in local time stepping mode (Tóth et al. 2012), which speeds up convergence toward a steady state solution. The solution is then further relaxed with an excessive amount of 200,000 iterations. We finally turn on the fifth-order solver and switch the simulation to the normal time accurate mode and relax for 36 hours of physical time, ensuring a true steady state while minimizing any possible artifacts from the local time stepping run.

3. Simulation Results and Comparisons

3.1. Simulation Results

We first present 3D results of the final steady state of our simulation run. Figure 2(a) shows the computational grid structures in the domain close to the Sun. As explained in Section 2.3, for the lower corona below 1.7 Rs and around the AR, extra levels of AMR are set. Interestingly, since AWSoM is a global solar model, along side the AR, we are able to model the coronal holes and magnetic field connections between the AR and the poles. The AMR region for the AR is also sufficiently large to cover any significant structures we would like to study and avoid potential discontinuities or other artifacts near the AMR boundary. We also see open field lines coming from near the east-side footpoint of the AR, while near the west footpoint, we see long loops connecting with the north pole. Figure 2(b) shows a topdown view at the AR. The solar surface (at 1.001 Rs) is colored by the radial component of the magnetic field. The magnetic field lines are colored with the logarithm of the wave dissipation (heating) rate (in unit [log W m⁻³]). For this weak AR, the structures are in general potential. However, because our AWSoM model is able to relax the solution to a MHD steady state, and because of the extra high resolution, we use in this simulation, we are also able to model the slight nonpotentiality in the magnetic field configuration. In addition, since the wave dissipation rate depends on the magnetic field strength, differences in heating rates for nearby loops (loop bundles) can be found (see below for visible differences in nearby loop brightness). We also find that the heating rate is in general higher for the closed field regions and small loops connecting the two footpoints, and lower for open field lines and larger loops. This is expected as the turbulent dissipation relies on oppositely propagating waves: the counterpropagating waves on the open field lines are generated only by wave reflection, while those on the closed field lines include both the reflected waves and the major waves coming from the other footpoint, which would naturally be stronger. Note that our model

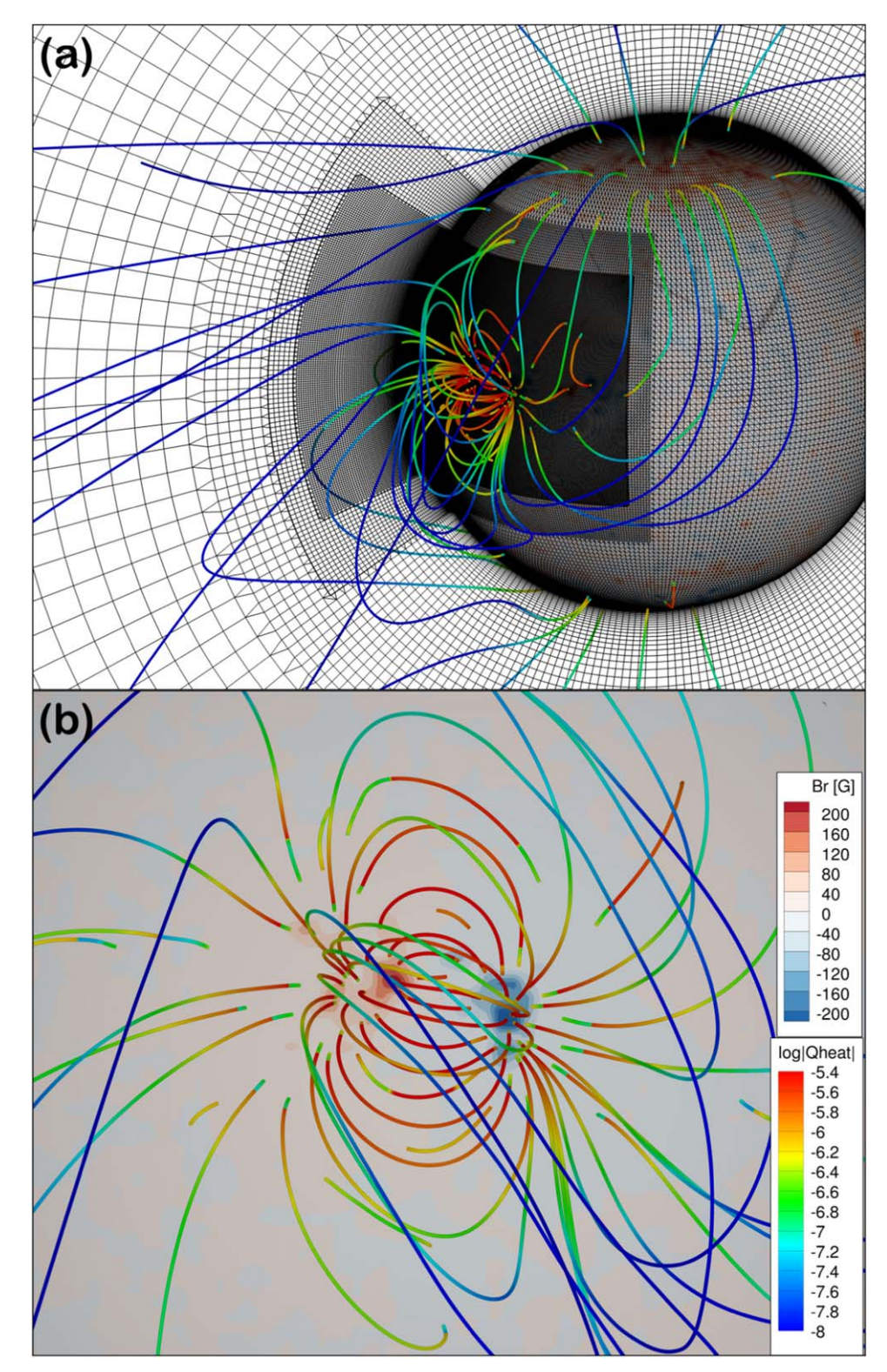


Figure 2. AWSoM simulation results: 3D views. (a) The computational grids we use, showing the increased AMR levels for the lower corona and the AR. (b) A top-down view for the AR. In both panels, the solar surface (at 1.001 Rs) is colored with the radial magnetic field, where the contour levels saturate at ± 20 G for panel (a) and ± 200 G for panel (b). Some zigzag patterns in (a) on the solar surface are plotting issues with the software and not present in the actual simulation. The magnetic field lines are also plotted in both panels and are colored with the logarithm of the wave dissipation (heating) rate (unit [log W m⁻³]; logarithms in this paper are all 10 based) with the legend in panel (b).

does not take into account another potential heating mechanism of uniturbulence, where the propagating Alfvèn waves nonlinearly self-deform (without the need of counter-propagating waves) and cascade to smaller scales in the presence of transverse

inhomogeneities (Magyar et al. 2017, 2019; Pant et al. 2019; Van Doorsselaere et al. 2020).

Figure 3 shows a side view of the AR. A meridional cut plane through the center of the AR is plotted with both colored

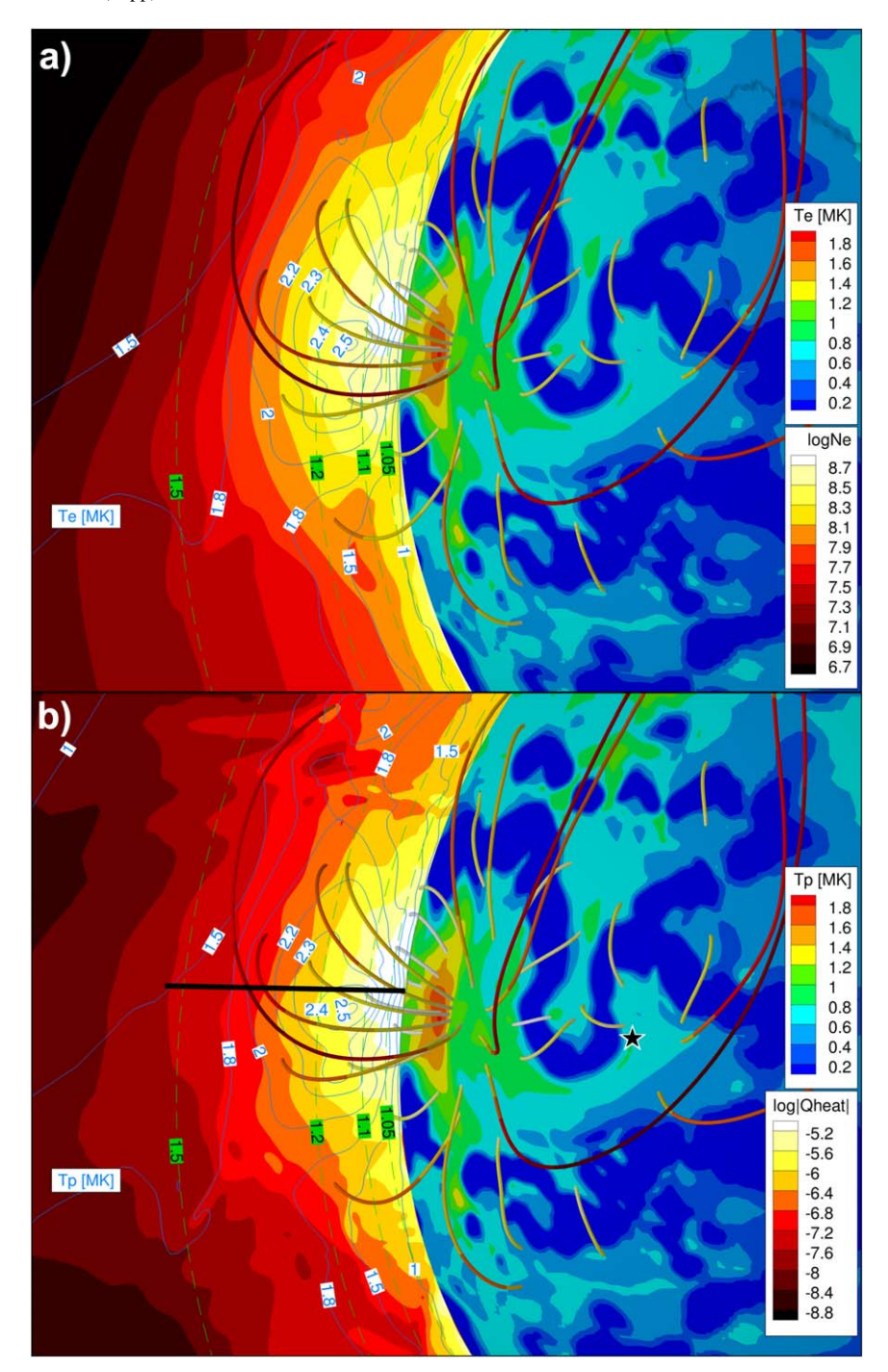


Figure 3. Side view of the AR. The spherical shell is plotted at 1.02 Rs. A meridional cut plane through the center of AR is also plotted. Radial distances are marked on the cut plane in green for reference. (a) The spherical shell is colored with T_e , and the blue contour lines on the cut plane are also for T_e , with the corresponding levels marked in blue. The cut plane is colored with plasma density N_e in unit [log cm⁻³]. The magnetic field lines are also colored with N_e . (b) The color on the spherical shell and the contour lines on the cut plane show T_p . The cut plane and the magnetic fields are colored with wave heating rate in unit [log W m⁻³]. The thick black line on the cut plane and the black star marked on the solar surface denote the locations that we extract the 1D density and temperature profiles. See text and next figure.

contours showing electron density (in panel (a)) and heating rate (in panel (b)), and contour lines showing the (a) electron and (b) proton temperature. The electron density (which is the same as proton density) is plotted in logarithm scale and unit [log cm⁻³]. The temperatures are in unit [MK] and the levels are marked on the corresponding contour lines in blue. Here the spherical surface is at an elevated radial distance of 1.02 Rs. The colors on the spherical surface show the (a) electron and (b) proton temperature. Note that the 3D view is tilted, and we

plot dashed lines marked with the radial distances in green as a reference. The magnetic field lines are also plotted as a reference. Immediately we notice that our AWSoM model creates a heated corona up to 2.5 MK with obvious structures in the AR. At 1.02 Rs, the footpoints (\sim 1.8 MK) are hotter than the center of the AR (\sim 1 MK), while higher up at 1.1 Rs, the AR loop top has the highest temperature of 2.5 MK.

AWSoM is also able to populate the AR with denser plasma. We find this to be a benefit of the combined effect of high grid

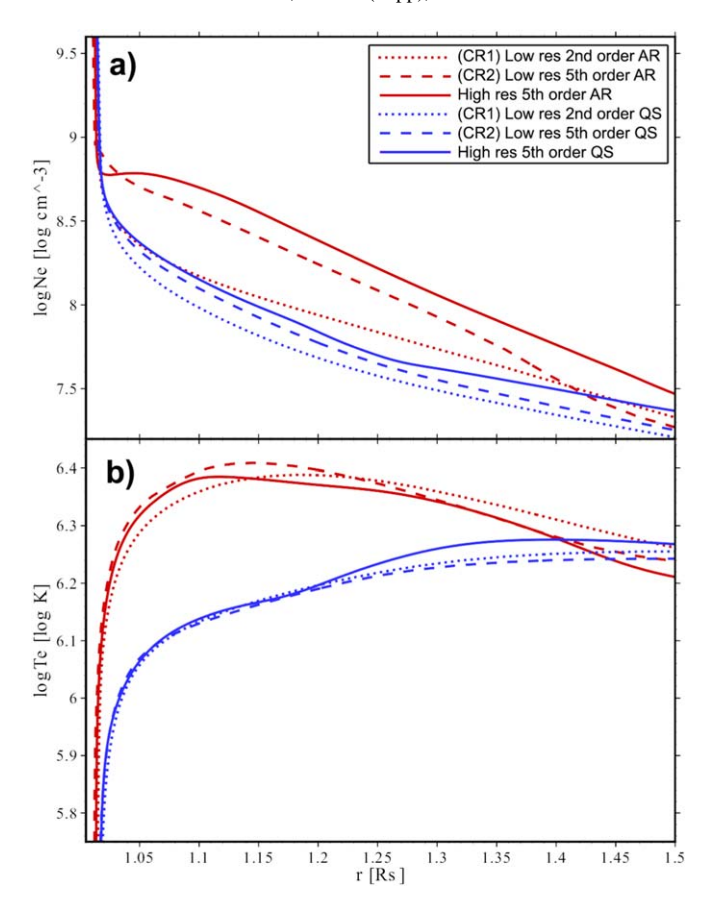


Figure 4. Extracted radial density and temperature profiles. Panel (a) shows the electron number density N_e , and panel (b) shows electron temperature T_e . The red lines are extracted through the center of AR (thick black line in Figure 3(b)). The blue lines are for the quiet Sun (black star in Figure 3(b)). The dotted lines show results from low-resolution comparison run, CR1, and the dashed lines show CR2. The solid lines show results of the high-resolution fifth-order run as described in Section 2.3. See text for more details.

resolution and the fifth-order scheme. Otherwise, the numerical diffusion is too strong, and these detailed density structures are mostly smeared out. We do two low-resolution comparison runs: (CR1) does not have the extra two levels of AMRs for AR (resulting in a horizontal resolution of 1.4) and uses only the second-order scheme for the entire run; and (CR2) has the same resolution as (CR1) but uses the fifth-order scheme for corona below 1.7 Rs. All the other parameters are set to be the same as the high-resolution run performed for this paper. All the runs are relaxed for 36 hours physical time. We extract two lines in the radial direction and plot the 1D density and temperature profiles in Figure 4. The red profiles are extracted through the center of the AR (as shown in Figure 3(b) as black thick line on the cut plane, with Carrington longitude 294° and latitude 4°.5). The blue profiles represent the quiet Sun (QS) and are extracted at the same latitude but 30° west from the AR, which is sufficiently far away from the core of the AR while still within our AMR boundary (location marked as a black star in Figure 3(b)). It can be seen that both the higher resolution and the fifth-order scheme help to reduce cross-field numerical diffusion and preserve a higher density in the AR. The increased resolution also prevents loss of Alfvén-wave energy by diffusion, so it sustains higher levels of turbulence and thus greater heating rates that balance the radiative loss of the denser AR. Here, we only aim to give readers a better view of the 1D density and temperature profile for our simulation result and to show the significance of the high resolution and the higherorder scheme. Detailed investigations and discussions about the comparison are left for our future work.

3.2. Global Solar Wind Structures and in Situ Comparisons

Next, we look at the global solar wind structures of our simulation. Figure 5 shows a meridional cut through the AR (same as the cut in Figure 3) for the full domain up to 24 Rs. The dashed red contour lines show the radial solar wind speeds (in unit $[km s^{-1}]$). The polar wind is accelerated to greater than 500 km s⁻¹, while structures of the streamer belt can be found near the equator plane (and the belt itself is slightly bent southward). The color-filled contours show the electron temperatures, while the blue contour lines show the proton temperature with the values labeled on the corresponding lines. At this large scale, although the electron temperature looks reasonable, the proton temperature appears to be suspicious, especially for the polar region. Above about 2 Rs, the proton temperature rapidly cools down and then increases, but is never able to exceed the electron temperature even at about 5 Rs. This is unlike observations and is also an unusual behavior for our AWSoM model (see van der Holst et al. 2014 for a typical AWSoM solution). The contour lines for proton temperatures also show many structures that appear to be questionable with our coarse resolution at this scale.

As a comparison, for the same CR, we change the input for our inner boundary to the Air Force Data Assimilation Photospheric Flux Transport (ADAPT)/Global Oscillation Network Group (GONG) synoptic map (Worden & Harvey 2000; Arge et al. 2010; Henney et al. 2012; Arge et al. 2013; Hickmann et al. 2015). While the electron temperature distribution for the new run is similar, the proton temperature now behaves as expected, as our typical results. See Discussion for more details. We present the conclusion here that the unusual behavior for the proton temperature at large scales in our simulation with the NSO/HMI map is due to the treatment of the polar region magnetic fields in the map. Although it limits the applicability of this simulation to large-scale studies that involve proton temperatures, it should not affect our current focus on the AR heating.

In order to better validate the solar wind results with observations, we do a simulation with the IH component of SWMF based on our SC steady state solution. We use a typical IH setup with a Cartesian domain in the Heliographic Inertial Coordinate System covering ± 250 Rs. The adaptive grid size ranges from 0.5 to 8 Rs, and the total number of cells is about 8 million. We use the OMNI (King & Papitashvili 2005) data to compare the solar wind measurements at 1 au. Figure 6 shows the observed (black) and simulated (red) plasma radial velocity, proton (electron) density, proton temperature, and magnitude of the magnetic field. It can be seen that all of the quantities from our simulation are in similar ranges as the observations, especially the proton density (at quiet times) and the magnetic fields. Since our focus of this study (and computational resources) is on the AR and at lower corona, the computational grids are very coarse (2°.8) above 1.7 Rs. No AMR has been set for the current sheets or near the Earth observer. It is already convincing for us that the simulated solar wind is close to observation, and we do not expect to match any of the exact values or detailed variations of the quantities. Interested readers may refer to Sachdeva et al. (2019) for typical performances for AWSoM with the IH component.

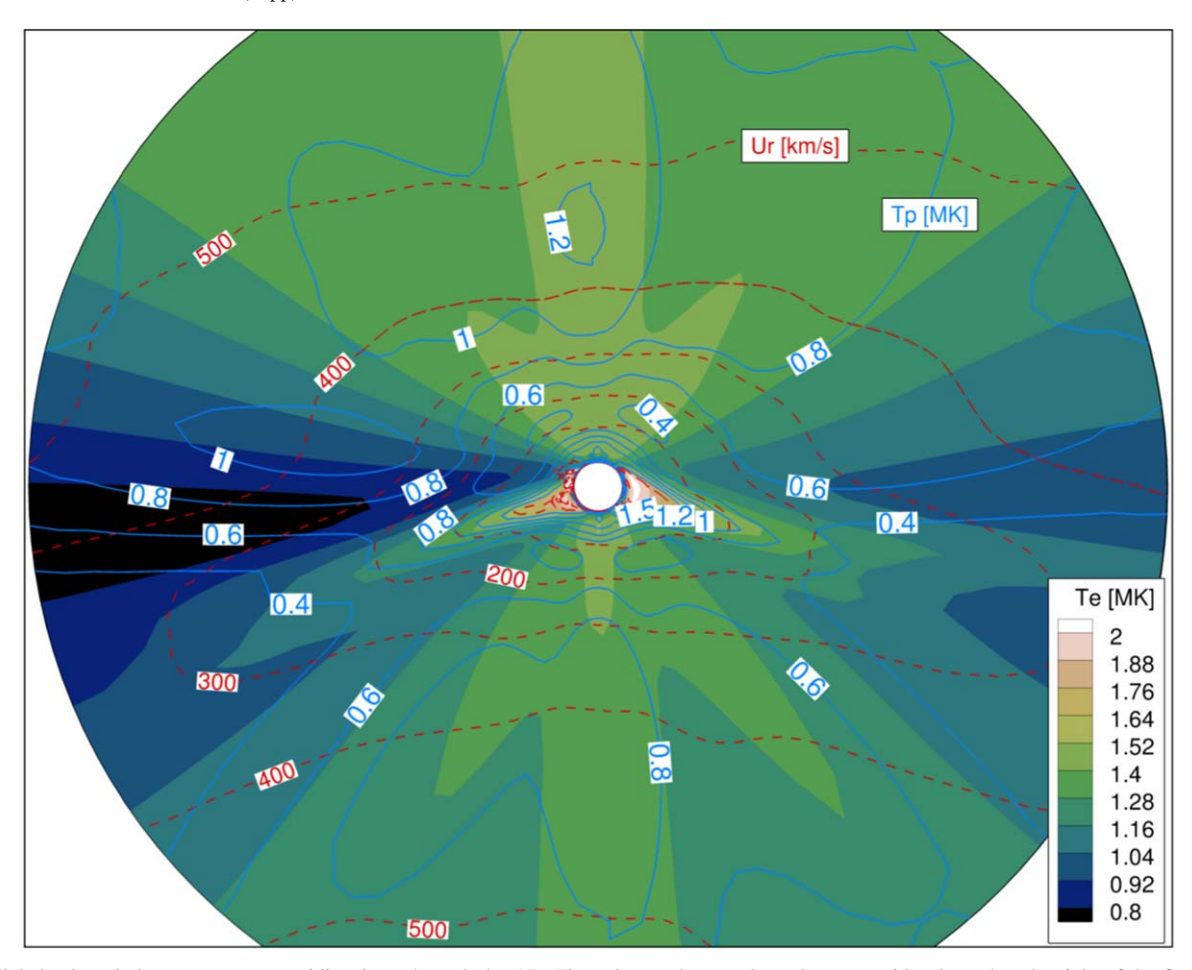


Figure 5. Global solar wind structures at a meridional cut through the AR. The color on the cut plane shows T_e with a legend to the right of the figure. The blue contour lines show T_p in unit [MK], with the levels marked on the corresponding lines. The red dashed lines contour the solar wind radial speed in unit [km s⁻¹].

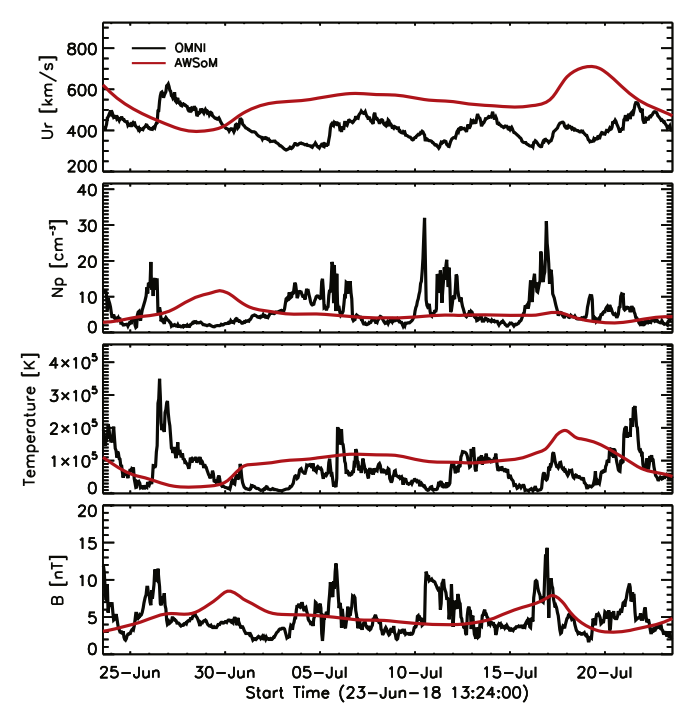


Figure 6. Comparisons between the modeled in situ quantities (red lines) and OMNI measurements (black lines) for CR 2206. The four quantities from top to bottom are as follows: radial velocity, proton density, proton temperature, and magnitude of the magnetic field.

Therefore, except for the unusual behavior of the proton temperature at the poles above 2 Rs, our solution provides reasonable solar wind results both below 24 Rs and at 1 au. Since our focus in this study is the AR structures well below 2 Rs where the electron and proton temperatures are similar and well behaved, we here justify the use of this solution and leave the question of the unusual global proton temperature results to future works. A future paper in this series will be discussing more about the solar wind both coming from the poles and near the AR and will also do an analysis of the ion charge states.

3.3. Spectrum Synthesis

For a detailed comparison with the observations, we synthesize spectral lines with the SPECTRUM code (Szente et al. 2019) and compare the results with the Hinode/EIS data. As opposed to the narrowband-integrated images, each spectral line is sensitive only to a very narrow range of temperatures and to the densest plasma. Therefore, from the synthesized line emissions, we are able to better understand and validate the modeled plasma temperature and density structures.

The SPECTRUM code utilizes our AWSoM simulation results with the two-temperature plasma to produce synthetic spectral lines. For this study, we updated SPECTRUM to use adaptive segments for the LOS integral of emissivity on the native spherical grid, so interpolation to a coarser Cartesian grid (see Szente et al. 2019) is no longer needed. Therefore, it

better accounts for the AWSoM's radially, highly stretched computational cells and finer resolutions in the AMR region.

To calculate the spectral line emissions, the plasma is assumed to be in ionization equilibrium, and the ion temperatures are assumed to equal the proton temperature. SPECTRUM then calculates the line intensities at each voxel with the electron temperature and density from the AWSoM model results. The contribution function available in the SPECTRUM code was precalculated with CHIANTI database version 8 (Del Zanna et al. 2015). We do not expect the results to change significantly with the latest version of CHIANTI (version 10; Del Zanna et al. 2021). Doppler-shifted spectral lines are then broadened with proton thermal velocity and the LOS Alfvén wave pressure. The spectrum is then integrated along the LOS for each pixel, assuming the plasma to be optically thin. We use the coronal element abundance that Feldman (1992) stored in the CHIANTI database, and currently, open and closed field regions are considered to share this same abundance.

For a better comparison with the EIS observations, we use the same observer LOS, FOV, and image resolution (binned down to 4'') as the EIS data. Note that, despite our best efforts, the finest grids in the code (0°.35 horizontal resolution, or about 6" near disk center) still struggle to catch up with the EIS resolution (see Ignacio Ugarte-Urra, 2016; EIS Software, Note 8; for 1" slit, the effective resolution is about 3" in both scan and slit directions). With the added resolvability of the fifthorder scheme, however, we are able to increase sharpness and reduce diffusion and roughly achieve 0°.1 (1".7) resolution, which is comparable to the EIS resolution. The problem is that the intrinsic resolution needed to simulate the subgrid structures is much higher. Therefore, we do not expect the simulation to match the pixel-level fine details in the EIS observation, but rather, we will mainly compare the large-scale structures, and spend more effort on quantitatively comparing the results. For the synthesis, we also use the same wavelength ranges and pixel size in Angstrom (0.0233 Å) as EIS. Besides the thermal and nonthermal line broadening, a constant 70 mÅ instrumental broadening is also added (and later removed from the fitted results).

To post-process the synthesized spectrum, we use the same line fitting procedures and spectral line templates (initial guess of the parameters for the fitting) as for the EIS observations. To obtain the photon count error as required by the line fitting program, we derive a very simple error measure from the EIS data as

$$E = \max(c, k\sqrt{I} + b), \tag{1}$$

where I is the observed emission at each pixel and wavelength bin, E is the corresponding noise count, c is the base noise level that is arbitrarily chosen from EIS data as the thirty-second smallest nonnegative noise count in the given wavelength range (to avoid occasional outliers or extraordinary values), and k and b are two coefficients that are linearly fitted from the EIS data. The three coefficients are fitted with all the data points in a given wavelength window, and are different for different wavelength windows. Note that this error measure is only to be used with the line fitting procedures, and has only a small effect on the fitted Gaussian profiles. In practice, this relationship gives us a pretty good error measure to use with the synthesized lines without relying too much on detailed knowledge of

instrument calibrations. In some regions for the synthesis, the calculated line intensities may be weaker than the modeled noise, and thus, are marked as missing pixels.

3.4. Full Disk Synthesis and Comparison to AIA

We first synthesize full disk images and compare them with the SDO/AIA observations. Usually, the synthesized AIA images are obtained by integrating the modeled plasma temperatures and densities with the estimated temperature response of the narrowband filters. However, with the SPECTRUM code, we are able to directly calculate the spectral line emissions and then integrate with the AIA-filter wavelength response to produce the final images. This method, although it requires more effort, preserves more details in the simulation results and gives a more realistic synthesis, especially for the AR loops (see below).

Here we briefly describe quantities and equations we use in synthesizing AIA observables with the wavelength response function. Detailed explanations of the instrument calibration processes can be found in Boerner et al. (2012). At a pixel x (on CCD) and for channel t, the AIA-observed value p (in units of digital number [DN]) can be written as

$$p(\mathbf{x}, t) = \int_0^\infty I(\mathbf{x}, \lambda) \eta(\mathbf{x}, \lambda, t) d\lambda, \qquad (2)$$

where λ is wavelength, $I(x, \lambda)$ is the spectral intensity over the solid angle of the specified pixel, and $\eta(x, \lambda, t)$ is the efficiency function of channel t of the telescope:

$$\eta(\mathbf{x}, \lambda, t) = A_{\text{eff}}(\lambda, t)g(\lambda)F(\mathbf{x}). \tag{3}$$

Here the effective area $A_{\rm eff}(\lambda,t)$ is derived from the efficiency of the telescope optics, and $g(\lambda)$ is the CCD gain. The flat-field function F(x), including vignetting, filter-grid shadowing, and CCD-sensitivity variations, is assumed to be unity for the synthesis. The AIA-EUV thin filter end-to-end instrument response function $R(\lambda,t) \equiv A_{\rm eff}(\lambda,t)g(\lambda)$ is provided by the SSW function $\text{aia_get_response}(/\text{area},/\text{dn})$. Version 8 of the AIA-filter wavelength response function is used. For ease of calculation, we only consider the significant portion of the response function around the requested wavelength (e.g., for 304 Å, outside of 280–330 Å, the response is set to zero).

Figures 7 and 8 show a comparison of the observations with the synthesis. AIA synthetic images that use the traditional approach with the precalculated temperature response functions are also included for reference. Each group of three images in a row in these two figures shows a channel of AIA (noted on the upper left corner). The three images are, from left to right, the AIA observation, the SPECTRUM synthesis with the wavelength response, and the synthesis with the traditional temperature response. We use the standard SSW function aia_intscale for the plots. The plotting range (maximum and minimum values) and scaling function applied (square root for 94 and 171, and logarithm for 131, 193, 211, 304, and 335 Å) are the same for three images within each group. Note that the 304 Å channel has a large contribution from chromospheric lines He II and cannot be considered as optically thin. Therefore, SPECTRUM code cannot synthesize this channel very well based on optically thin assumption. Instead, we synthesized only one spectral line: O V 265.551 Å, with a maximum formation temperature (here we define as the temperature of the peak of the contribution function) of

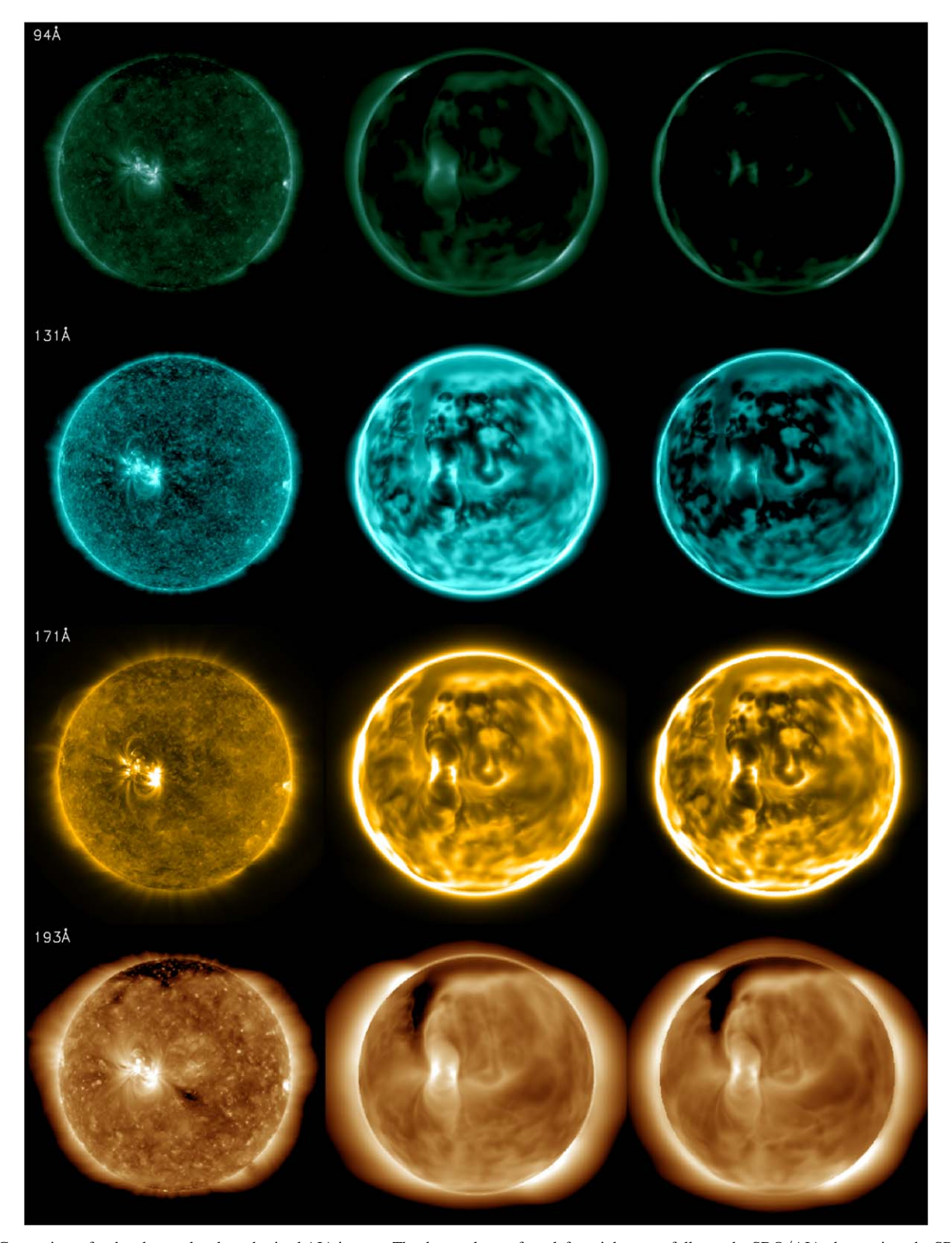


Figure 7. Comparisons for the observed and synthesized AIA images. The three columns from left to right are as follows: the SDO/AIA observation, the SPECTRUM synthesis with wavelength response, and the synthesis with traditional temperature response. Each row shows a wavelength channel that is noted on the upper left corner. All three images in each row are scaled with the same intensity range (using SSW function aia_intscale).

 $\log T_e^G = 5.4$ that is as close as possible to the chromosphere/transition region temperatures, so that the model's ability at capturing transition region morphology can be assessed. The second plot in Figure 8(304 Å) shows this O V line intensity, and, because of the different quantity plotted, this image has a

different plotting range from the other two 304 $\hbox{Å}$ images in Figure 8.

Overall the synthesis compares favorably to the observation. The locations of the coronal hole and AR are well captured. A larger northern coronal hole and a smaller southern one can be seen. We

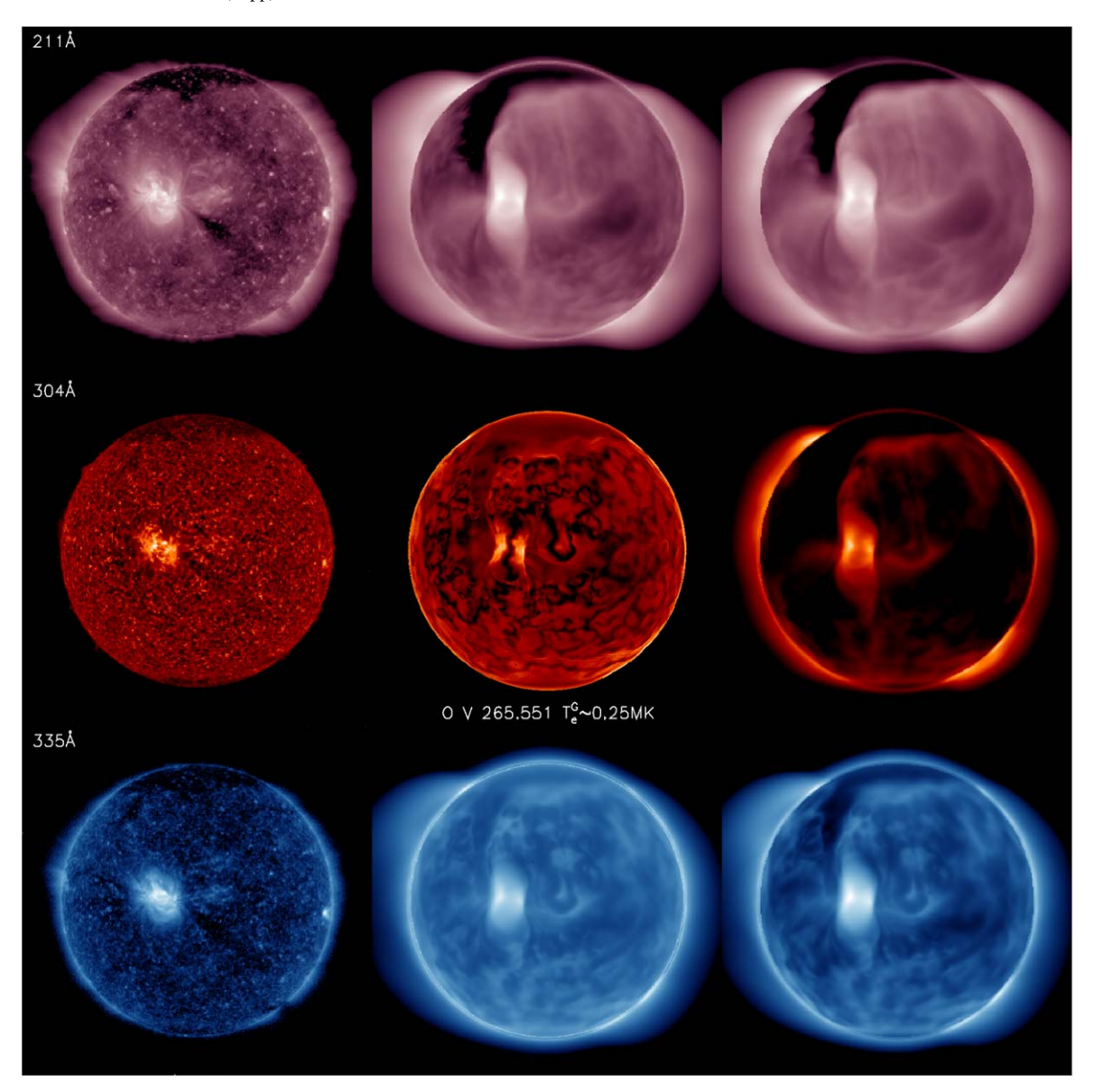


Figure 8. Comparisons for the observed and synthesized AIA images (continued for Figure 7) for the other three channels. Here the SPECTRUM synthesized 304 Å is replaced with synthesized O V 265.551 Å line intensity ($T_e^G \approx 0.25$ MK; image not scaled the same as the other two). This better represents the chromospheric He II lines that are not optically thin.

see signs of an extended (to lower latitudes) northern coronal hole in SDO/AIA images (especially for 193 Å), where our simulation also shows that the northern coronal hole may actually extend close to the east footpoint of the AR. Our synthesized coronal holes generally appear darker for all the wavelength channels than observation, which could be partially due to a lack of scattered light in SPECTRUM synthesis. It is also interesting to future studies to quantitatively evaluate our model performance on a coronal hole. Also note that the extended northern coronal hole is less pronounced (closer to observations) in images synthesized with SPECTRUM than in those with the traditional temperature response (for channels of, say, 193 Å and 335 Å).

We notice that the SPECTRUM result has larger intensities for 131 Å and 171 Å. These two channels both have low-temperature components (Fe VIII at $\log T = 5.6$ for 131 Å and Fe IX at $\log T = 5.8$ for 171 Å). The stronger intensities in these two channels are due to AWSoM model producing too large density for the low-temperature plasma (the effect can also be

seen below for the synthesis of cooler spectral lines). However, this is an expected behavior with the extended transition region in our model. Because of the extremely large gradients in the transition region and limited computational resources, despite our best efforts in using stretched radial grids and extra AMR levels to get a higher radial resolution, the modeled transition region still extends to higher altitudes and pushes the corona outwards. In addition, we use an overestimate of density at the inner boundary to prevent the excessive chromospheric evaporation (Lionello et al. 2009; Sachdeva et al. 2019). Therefore, we will get overdense plasma at cooler temperatures near our extended upper transition region, but as seen below, our coronal solution is generally not affected.

3.5. Detailed Active Region Comparisons

Now we start to examine in detail our model performance with a set of strong spectral lines covering a wide coronal temperature range. Figure 9 shows the comparison of EIS

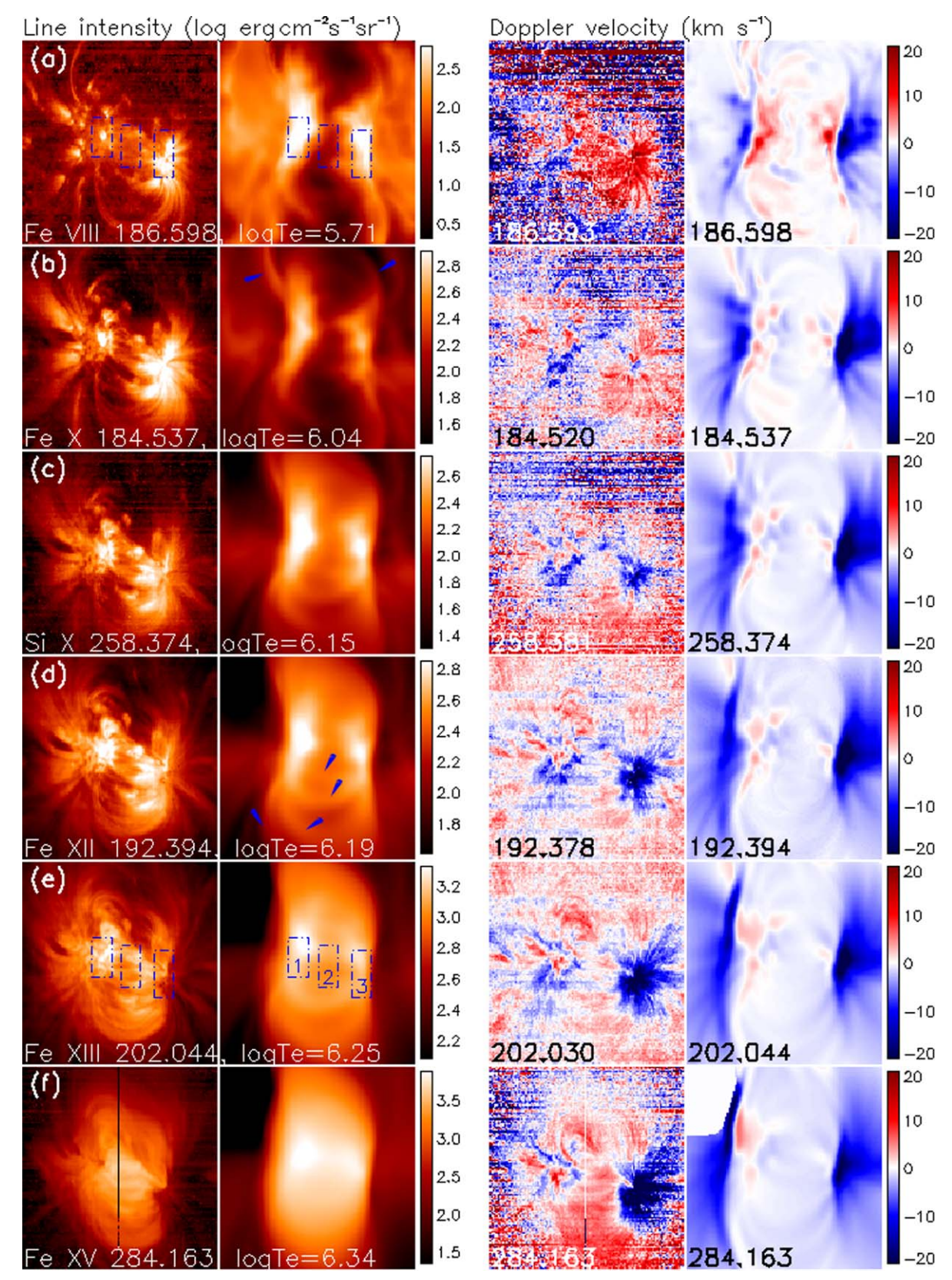


Figure 9. Synthesized spectral line intensities comparing to Hinode/EIS observations. The six rows correspond to the six selected spectral lines. In each row, from left to right, are EIS-observed line intensity, SPECTRUM synthesized intensity, EIS Doppler velocity, and SPECTRUM Doppler velocity. The spectral lines are labeled on the corresponding intensity images. The Dopplergrams calculated for the EIS observation use relative line centroids. The Dopplergrams for the SPECTRUM synthesis use absolute (theoretical) line centroids. The line centroids used are marked on the corresponding Dopplergrams. In panels (b) and (d), blue arrows mark some bundles of brighter loops. In panels (a) and (e), three boxes are drawn to indicate the three regions of interest: (1) east footpoint, (2) loop top, and (3) west footpoint. The locations for all the corresponding boxes are the same for all the images, but are only drawn in these two panels for clarity.

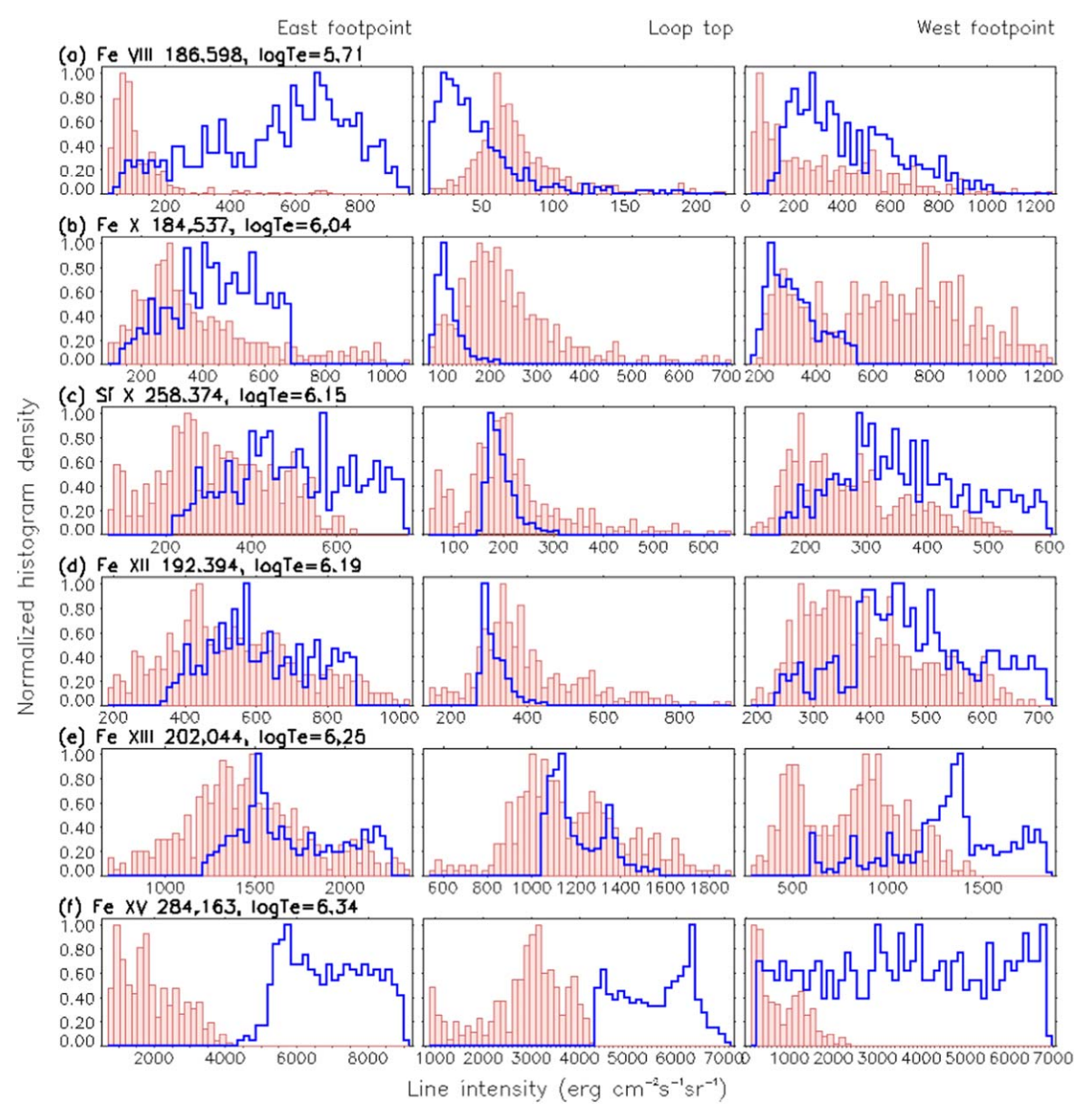


Figure 10. Normalized histograms comparing line intensities for observation (bars) and synthesis (blue lines). The three columns are, from left to right, the east footpoint, loop top, and west footpoint, corresponding to box regions 1, 2, and 3, respectively, as in Figure 9.

observations and SPECTRUM synthesis. The first two columns show the EIS and AWSoM spectral line intensities, respectively, in logarithmic scale. The minimum and maximum values of the two images are the same, with a colorbar plotted on the right. The following two columns are the fitted Doppler velocities, and they are both scaled from -20 to 20 km s⁻ Each row in Figure 9 shows a different spectral line marked at the lower left corner. The value shown following the ion and wavelength is the logarithm of the maximum formation temperature (T_e^G) of the corresponding line. The six EIS lines selected here are strong lines without nearby blends, and these lines have relatively less noise or missing pixels when compared to the rest of the spectrum. For the Dopplergram, currently it is very difficult to absolutely calibrate the EISobserved spectral line centroids. Therefore, besides our effort of correcting the spacecraft drift (discussed in Section 2), the standard procedures are used, and for each spectral line, we can

only get a relative line centroid that aims at providing a Dopplergram that averages to be zero over the entire image. The obtained relative wavelengths are noted at the lower left corner of the corresponding Dopplergrams of the observation, and they may not be the same as the theoretical ones. Note that the synthesized Dopplergrams are absolutely calibrated (using the theoretical wavelengths) to provide a better sense of our model performance and a potentially more realistic picture of the AR.

Spectral lines with different formation temperatures sample the solar atmosphere at different altitudes. By comparing the observed and synthesized line intensities, we are able to compare the plasma densities in different structures. For a quantitative study, we also select three box regions corresponding to the east footpoint, loop top, and the west footpoint. The boxes are plotted in Figure 9. In Figure 10, a comparison of the histograms of the line intensities within three box regions

 Table 1

 Relative Difference between Synthesized and Observed Spectral Line Intensities

Spectral Line	T_e^G (MK)	East Footpoint ^a	Loop Top ^b	West Footpoint ^c
Fe VIII 186.598	0.51	361.2%	-39.3%	33.0%
Fe X 184.537	1.10	15.6%	-53.2%	-50.1%
Si x 258.374	1.41	56.7%	-9.2%	34.0%
Fe XII 192.394	1.55	14.7%	-20.9%	21.5%
Fe XIII 202.044	1.78	17.4%	2.1%	64.3%
Fe XV 284.163	2.19	258.6%	96.9%	371.3%

Notes. The regions used are the same for all the spectral lines. Relative difference is calculated as synthesis divided by observation, then minus one.

and for all six spectral lines is shown. Table 1 shows the relative error of our synthesis for the averaged line intensity within each box.

For cooler lines, such as the Fe VIII 186.598 Å, we mostly see the bright footpoints in the EIS observation (Figure 9(a)). The locations of the footpoints are reproduced by the simulation well. However, the east footpoint we get is 4 times brighter than what is observed (Table 1). Our quiet region is also producing higher emission than the observation. For warm temperatures $T_e = 1.1 - 1.8$ MK, our model matches the observation to a very good degree; see synthesized line intensities of Si X, Fe XII, and Fe XIII. As shown by the quantitative comparisons in Table 1, the relative differences between the observed and synthesized line intensities are generally less than about 50%, with some of them being as close as less than 20%. For these warm lines, the emissions mostly come from the AR loops, and the small loops between the two footpoints start to show up. For the higher-temperature lines (say, Fe XV 284.163 Å) greater than 2 MK, the AR loops produce most of the emission. The top of the small loops between the two footpoints show the largest brightness. We also see less contrast for the coronal loops where the loop threads are not as clearly seen as in the warmer lines, and the entire AR appears as a fuzzy blob of brightness. The synthesized emission is 2 times (4 times) larger for the loop top (footpoints) than the observation.

Overall, our simulation reproduces the observed morphology, and matches line intensities for both the AR loops and the footpoints extremely well with less than 50% error for most of the cases. The AWSoM results compare the best for warm temperatures around 1.5 MK, where we start to see the bright loop tops showing up in the spectral observations. The line intensity histograms of these warm lines for the synthesis are also very close to those for the observations. The synthesized images show enhanced intensities for some of the loops connecting the two footpoints, as well as indications of fan loops extending outwards from the footpoints. These bright and dark loop bundles tracing our magnetic field lines from the synthesized images generally match the observed morphology (see blue arrows in Figures 9(b) and (e)). In our Alfvén wave heating model, the dissipation rate for the wave energy density is proportional to the square root of the magnetic field strength. Due to magnetic field structures at the footpoints (and thus along the loop), even spatially nearby loops may have a different amount of Alfvén wave dissipation at the footpoints and thus along the loops. Therefore, loops with larger magnetic fields will naturally have more heating and show up in different temperature channels, which can be easily picked up by the

highly sensitive spectral line synthesis. These results are only possible because we achieve a high spatial resolution for the simulation and actually resolve the magnetic field structures in the synoptic map at the inner boundary.

The model-observation differences are as follows. We find that the model produces larger emission at lower temperatures for the quiet regions, indicating that the simulated upper transition region/lower corona is too dense. As discussed above, this is an expected behavior with the extended transition region in our model. We may need to further increase the computational grid resolution to overcome this issue with the too dense transition region. It also seems that our model heats up the loop tops to a slightly too high temperature. In fact, from Table 1, we find that we underestimate the loop top intensities for the four lower-temperature lines but overestimate that for the two higher-temperature lines. Nevertheless, AWSoM does perform very well to match the general morphology and structures with the observation. There is one free parameter of the Poynting flux (per magnetic field strength) that controls the Alfvén wave energy we inject at the solar surface; currently we use a value (0.5 MW m⁻² T⁻¹) that is derived from the historical observations and empirically performing well for our validation studies for the solar maximum (see Sachdeva et al. 2021; also see Sachdeva et al. 2019 for studies of solar minimum). Reducing that value may help produce even better matches to some of the observed line intensities. A follow up paper is in progress showcasing the effect of Poynting flux on our simulation results.

Now let us examine the Dopplergrams. The most noticeable feature in the observed Dopplergram is the blueshifts near the west side of the AR. As clearly visible, the blueshifted region is relatively small in Figure 9(c) for Si X line at 1.41 MK, and the region size as well as the magnitude of LOS velocity gradually increases for Figures 9(d), (e), and (f). The expansion of the blueshifted region and the increase of velocity with the increase of temperature (i.e., altitude) indicates the expansion of the open field lines and the acceleration of the solar wind. A slightly darker region toward the west side of the west footpoint is also visible in the AIA observation (Figure 7(193 Å)), suggesting open fields or some outflows. Interestingly, in the simulation result, we are unable to find any open field lines near the west footpoint, but instead, we find long loops connecting the AR and the north pole (Figure 2(a)). It suggests siphon flows on the very long loops connecting an AR and a pole, which we then confirm in the 3D-simulation data.

Outside of the east footpoint, we also find blueshifted regions. Here in the observation, the blueshifts are not as large in region size nor as strong as found for that at the west

^a The region is shown in Figure 9(e) as boxed area with number 1.

^b Boxed area number 2.

^c Boxed area number 3.

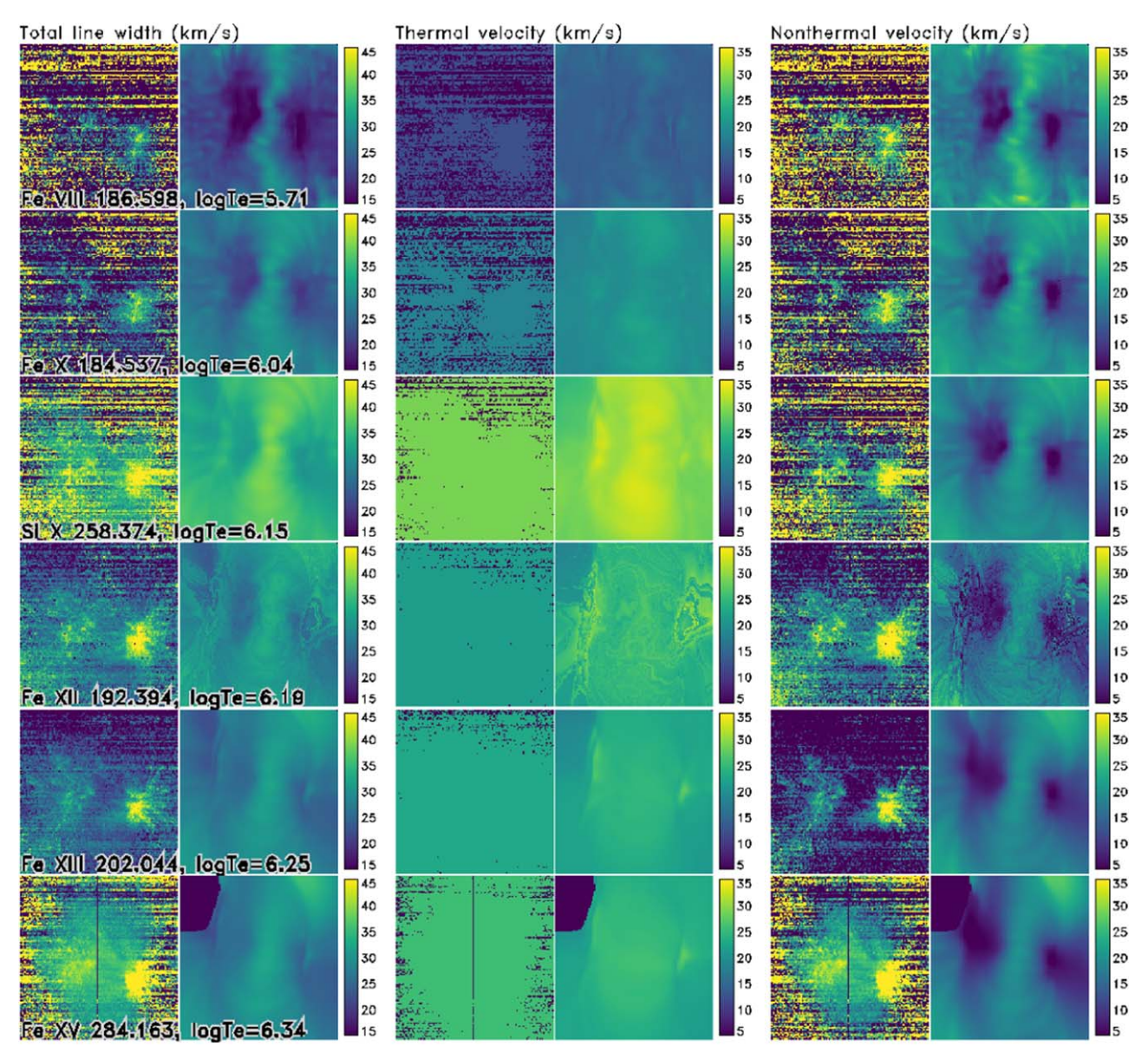


Figure 11. Comparison of observed and synthesized line widths. Each row is one of the selected spectral lines marked on the lower left corner in the same order as in Figure 9. In each row, the six images, from left to right, are (1) EIS total line width, (2) synthesized total line width, (3) and (4) EIS and synthesized thermal width, and (5) and (6) EIS and synthesized nonthermal width.

footpoint. Our synthesis reproduces this feature very well. Note that for the observations of Fe XII 192.394 (Figure 9(d)) and Fe XIII 202.044 (Figure 9(e)), the relatively calibrated line centroids are both smaller than the theoretical ones, so the actual Dopplergrams may be more blueshifted. Therefore, the EIS observation supports our finding of the open field lines with the outflows near the east footpoint.

3.6. Nonthermal Line Broadening

The spectral line width (after the instrumental broadening is removed) can be written as

$$\frac{c}{\lambda_0} \frac{\Delta \lambda}{2\sqrt{2 \ln 2}} = \sqrt{\frac{k_B T_i}{m} + v_{\text{nth}}^2} \equiv \sqrt{v_{\text{th}}^2 + v_{\text{nth}}^2} \equiv v_{\text{total}}, \quad (4)$$

where $\Delta\lambda$ is the full width at half maximum of the (assumed) Gaussian profile of the line, λ_0 is the rest wavelength, c is the

speed of light, k_B is the Boltzmann constant, T_i is the temperature of the emitting ion, m is the ion mass, and $v_{\rm nth}$ is the nonthermal velocity. For a better line width comparison between different lines, thermal $(v_{\rm th})$ and total line width $(v_{\rm total})$ expressed in velocity units are also used.

Figure 11 shows the comparisons for line widths for the same set of spectral lines shown in Figure 9. The first two columns are the total line broadening (with instrumental broadening removed) for the EIS observation and SPECTRUM synthesis, respectively. The EIS and synthesis are scaled to the same plotting range with the legend shown on the right.

For the observation, currently it is not possible to directly observe only the ion temperature or separately measure the thermal and nonthermal line widths. Therefore, assumptions about the thermal or/and nonthermal line width need to be made. A common assumption is that the ion temperature (T_e) equals the electron temperature (T_e) where the contribution

function of the corresponding line reaches the maximum. By assuming $T_i^{\text{obs}} = T_e^G$, the thermal line width is a constant everywhere for each spectral line. The nonthermal line width can then be calculated by removing the thermal line width from the total line width.

For the simulation, since we have all the 3D information about the plasma, we are able to separate the effect between the thermal and nonthermal broadenings. Because the AWSoM simulation we have here is using a two-temperature model, T_i is assumed to be the same for all the ions and equals the proton temperature $(T_i^{\text{sim}} \equiv T_p^{\text{sim}})$. Two SPECTRUM synthesis are done: one with only thermal broadening and the other with both the thermal and nonthermal broadenings caused by the Alfvén waves. The first synthesis is fitted with the EIS auto fitting code to provide the (LOS-integrated) thermal line width, which is just the total line width in this run, since we only include the effect of the thermal broadening here. The second synthesis is then used to provide the actual total line width, and by removing the thermal line width that we obtained from the first run, we can get the nonthermal line width for the simulation. Note that the LOS-integrated line profile represents only an average state of the plasma: if the stratified plasma is not isothermal or has varying Doppler shifts along LOS, the integrated thermal width may be different from that calculated from the maximum formation temperature, while the nonthermal line width may be affected by varying Alfvén wave amplitudes, and the densest voxels will give the largest contributions. Caution should be taken when analyzing such LOS-integrated data (De Moortel & Pascoe 2012; Pant et al. 2019).

We now look closer to the thermal temperatures. Comparing the thermal widths between the observation and simulation, we notice that $T_i^{\text{sim}} > T_i^{\text{obs}} \equiv T_e^G$. Landi (2007) carefully analyzed the Solar and Heliospheric Observatory's (Domingo et al. 1995) Solar Ultraviolet Measurement of Emitted Radiation (Wilhelm et al. 1995) data and also suggested that the ion temperature range lies significantly higher than the measured electron temperature in several cases (also see Seely et al. 1997; Tu et al. 1998 for similar conclusions). The difference between thermal widths shown in Figure 11 suggests that our simulation may have actually captured this ion (proton) temperature, which is higher than the maximum formation (electron) temperature of the spectral lines. However, from the simulation results (see Figure 3), we find that proton temperatures, especially within the AR and for the small loop tops, are less than 1% different from the corresponding electron temperatures. In fact, in these dense regions in the AR, collisions are abundant to effectively smooth out the differences between T_e and T_p . Therefore, the apparent higher thermal widths found for the synthesis for all six lines are most likely due to a combination of contribution function sensitivities, plasma density distribution, and LOS integration effects.

Comparing the nonthermal widths, we immediately notice that the results are very different. Because the only source of nonthermal broadening in our simulation is the Alfvén waves, the nonthermal velocities are concentrated only near the loop tops where the transverse waves are able to align with the LOS. Without longitudinal waves, almost no nonthermal broadening occurs at the footpoints where the magnetic field direction aligns with the LOS. On the other hand, despite our very rough assumption on the ion temperature, it is clear that the nonthermal broadenings in the observation are mostly

concentrated near the footpoints. It is an indication that compression waves, and wave mode conversions would further improve our coronal model (see below for discussions). In addition, our simulation does not capture reconnection outflows, which may also be responsible for the nonthermal broadening at the footpoints (e.g., Doschek et al. 2007; Baker et al. 2009; Tian et al. 2014; Cheng et al. 2015).

4. Summary and Discussion

In this work, we do an unprecedented validation study of the AWSoM model employing detailed spectral line comparisons to better understand the viability of the Alfvén wave turbulence-based coronal heating and solar wind acceleration. The simulation is done with extra levels of grid refinements that we have never reached before in our prior work, along with the latest developed fifth-order numerical scheme in the lower corona. This study is unique as it models the solar atmosphere in a global context, capturing the large-scale connections between the AR and the poles and open fields from near the AR, while also achieving high resolution within the AR, providing us with a tremendous amount of details. We first synthesize the full disk EUV observables to compare the largescale structures with SDO/AIA. The location and intensity of the solar structures, including the coronal holes, quiet regions, and the AR, compare favorably with the observations. We then focus on studying the AR (HARP 7283) near the disk center. Instead of using narrowband EUV synthesis that have information integrated and entangled, we use the SPECTRUM code based on the CHIANTI database to synthesize realistic spectral lines and directly compare to Hinode/EIS spectral observations. The line intensities compare favorably to the observations for a wide range of temperatures from 0.5 to 3 MK. For most of the cases (especially warm temperatures around 1.5 MK), the relative errors between synthesis and observation are less than 50%. It demonstrates that our MHD turbulence model with partial wave reflections and nonlinear stochastic heating is able to heat the corona, especially the AR loops, to a proper temperature that corresponds to what is observed.

To synthesize the EUV images of SDO/AIA, we use the SPECTRUM code to calculate a full spectrum for the solar disk and integrate with the effective areas of the narrowband filters. Although computationally more expensive, the results obtained by this method should be a better indicator of the true model performance, because the traditional temperature response functions require an assumption of either a fixed density or the pressure to calculate the line emissivities, which may be close to reality in general for most of the quiet regions but will not produce correct results for, say, AR loops with both elevated temperatures and densities. We find that the synthesized images compare very well with the AIA observations, both for the general morphology of various large-scale structures and even the observed intensities. Our results best compare to AIA images for the warm temperatures (\sim 1.5 MK), especially with the 193 Å line. It demonstrates that our AWSoM model has the capability of capturing the global structures for the solar atmosphere by providing a realistic full disk remote-sensing synthesis (as well as realistic 1 au predictions). The differences between our synthesis and the observation are mainly in the channels that include lowertemperature lines, where our (overdense) extended transition region results in too large intensities.

We do spectroscopic synthesis with SPECTRUM code and quantitatively compare the spectral line intensities with Hinode/EIS observations. The selected spectral lines cover a wide range of temperatures from 0.5 to 3 MK. We select regions for the two footpoints and the loop top and compare the histogram of line intensities as well as the average values. Our simulation matches very well with the observation, with relative errors less than 50% for most of the cases. We achieve the best result for Fe XII line at a maximum formation temperature of 1.55 MK, with relative errors of about 20% for all three regions of interest. We also compare the Doppler velocities, where we are able to find siphon flows in the long loops connecting the AR and the north pole, and also open field lines near the east footpoint of the AR.

Our simulation results suggest that the Alfvén wave turbulent heating alone does not seem to generate enough nonthermal line width near the loop footpoint. The longitudinal modes generated by compressive effects, mode conversion, or other mechanisms may be an important part in explaining such differences (Van Doorsselaere et al. 2020). Asgari-Targhi et al. (2014) used a 3D Alfvén wave turbulence model (van Ballegooijen et al. 2011; Asgari-Targhi & van Ballegooijen 2012; Asgari-Targhi et al. 2013) to study the coronal loop heating. They modeled and compared the nonthermal line widths with Hinode/EIS observations and also found a deficit of nonthermal broadenings for the model at the loop footpoints. In order to fit the observed nonthermal line widths, artificial parallel widths had to be added to the simulation results. Some of these parallel widths are up to 3 times larger than the perpendicular widths caused by the Alfvén waves.

In summary, AWSoM is capable of modeling a detailed AR embedded in the global SC with the state-of-the-art Alfvén wave turbulent heating, and can provide realistic observables for both EUV and spectroscopic images and 1 au measurements. Here we discuss some of the model limitations and recommendations for future work. In this study, we mainly focus on the lower corona and the AR, where collisions are abundant and the electron and proton temperatures are almost the same. However, as mentioned above, at larger altitudes beyond 2 Rs, the proton temperature behaves unusually. When the simulation run is repeated with the same parameters but with ADAPT/GONG synoptic map of the same CR, the polar proton and electron temperatures appear to be correct (for a validation study of AWSoM with ADAPT maps, see Sachdeva et al. 2019). The questionable low proton temperature for the polar regions is likely to be a problem with the enhanced polar magnetic fields of the NSO/HMI synoptic map. Due to observation limits, the magnetic fields for latitudes larger than 80 degrees have high uncertainties and may be missing when we are facing the inclined solar rotational axis. However, we emphasize here that our focus in this study is the AR and lower corona, where collisions are abundant and electron and proton temperatures are almost the same. For studying the AR, the NSO/HMI map naturally has higher spatial resolution and provides in general better details as compared to the ADAPT/ GONG map. Except for the proton temperature, the global solar wind plasma density and speed in our solution are as expected, and the measured values at 1 au align with OMNI observations very well. Thus, while we do recommend the interested modelers to use the NSO/HMI maps for simulations of ARs with AWSoM, cautions are needed and the proton temperatures should be examined in the context of global solar wind

structures. Extra steps in post-processing the magnetic fields in the polar regions of the synoptic map may also be helpful. The synthesized EUV images with SPECTRUM exposed some of the issues with too high density for our transition region, which would be interesting to address in the future. We may need even higher grid resolution and more computational power to fully resolve the narrow transition region. In addition, we assumed ionization equilibrium at local temperatures with the current version of the SPECTRUM code. Although we separate proton and electron temperatures, ion temperatures are not modeled and assumed to be the same as the proton temperature. Our previous study has already found that the nonequilibrium ionization effects can be important for lighter elements as well as higher charge states of Fe even below 1.5 Rs (Shi et al. 2019). We also assume the same element abundance for both the closed and open regions, ignoring the FIP effect (Feldman 1998; Laming 2015). For a full treatment of different ion temperatures, abundances, and nonequilibrium ionization effects, new developments for the AWSoM multifluid model are needed, and are currently an ongoing work (Szente et al. 2022).

We thank the anonymous referee for the comments, which helped us improve the original manuscript. This work was supported by NASA grants NNX17AD37G, 80NSSC20K185, 80NSSC18K1208, NNX16AL12G; NSF PREEVENTS grant 1663800; and NESSF grant 80NSSC17K0453. Resources supporting this work were mainly provided by the NASA High-End Computing (HEC) Program through the NASA Advanced Supercomputing (NAS) Division at Ames Research Center. We also would like to acknowledge high-performance computing support from Cheyenne (doi:10.5065/D6RX99HX) provided by NCAR's Computational and Information Systems Laboratory, sponsored by the National Science Foundation. CHIANTI is a collaborative project involving George Mason University, the University of Michigan (USA), University of Cambridge (UK), and NASA Goddard Space Flight Center (USA). The National Solar Observatory is operated by the Association of Universities for Research in Astronomy, Inc. (AURA), under cooperative agreement with the National Science Foundation. Hinode is a Japanese mission developed and launched by ISAS/JAXA, with NAOJ as domestic partner and NASA and UKSA as international partners. It is operated by these agencies in cooperation with ESA and NSC (Norway). Solar Dynamics Observatory (SDO) is the first mission to be launched for NASA's Living With a Star (LWS) Program. The data from the SDO/HMI and SDO/AIA consortia are provided by the Joint Science Operations Center (JSOC) Science Data Processing at Stanford University. The OMNI data were obtained from the GSFC/SPDF OMNIWeb interface at https://omniweb.gsfc.nasa.gov.

ORCID iDs

Tong Shi https://orcid.org/0000-0002-0827-7632 Ward Manchester IV https://orcid.org/0000-0003-0472-9408 Enrico Landi https://orcid.org/0000-0002-9325-9884 Bart van der Holst https://orcid.org/0000-0001-5260-3944 Judit Szente https://orcid.org/0000-0002-9465-7470 Yuxi Chen https://orcid.org/0000-0001-7288-2805 Gábor Tóth https://orcid.org/0000-0001-8459-2100 Luca Bertello https://orcid.org/0000-0002-1155-7141 Alexander Pevtsov https://orcid.org/0000-0001-9746-9937

References

```
Alfvén, H. 1947, MNRAS, 107, 211
Arge, C. N., Henney, C. J., Hernandez, I. G., et al. 2013, in AIP Conf. Proc.
   1539, Solar Wind 13 (Melville, NY: AIP), 11
Arge, C. N., Henney, C. J., Koller, J., et al. 2010, in AIP Conf. Proc. 1216,
   12th Int. Solar Wind Conf. (Melville, NY: AIP), 343
Aschwanden, M. J. 2019, New Millennium Solar Physics, Vol. 458 (Berlin:
   Springer), 238
Asgari-Targhi, M., & van Ballegooijen, A. A. 2012, ApJ, 746, 81
Asgari-Targhi, M., van Ballegooijen, A. A., Cranmer, S. R., & DeLuca, E. E.
  2013, ApJ, 773, 111
Asgari-Targhi, M., van Ballegooijen, A. A., & Imada, S. 2014, ApJ, 786, 28
Baker, D., van Driel-Gesztelyi, L., Mandrini, C. H., Démoulin, P., & Murray, M. J.
   2009, ApJ, 705, 926
Bavassano, B., Dobrowolny, M., Mariani, F., & Ness, N. F. 1982, JGR,
   87, 3617
Belcher, J. W., & Davis, L. 1971, JGR, 76, 3534
Boerner, P., Edwards, C., Lemen, J., et al. 2012, SoPh, 275, 41
Bogdan, T. J., Carlsson, M., Hansteen, V. H., et al. 2003, ApJ, 599, 626
Bogdan, T. J., Rosenthal, C. S., Carlsson, M., et al. 2002, AN, 323, 196
Chandran, B. D. G., Dennis, T. J., Quataert, E., & Bale, S. D. 2011, ApJ,
   743, 197
Chandran, B. D. G., & Perez, J. C. 2019, JPIPh, 85, 905850409
Chen, Y., Tóth, G., & Gombosi, T. I. 2016, JCoPh, 305, 604
Cheng, X., Ding, M. D., & Fang, C. 2015, ApJ, 804, 82
Coleman, P. J. 1968, ApJ, 153, 371
Cranmer, S. R. 2009, LRSP, 6, 3
Cranmer, S. R., van Ballegooijen, A. A., & Edgar, R. J. 2007, ApJS, 171, 520
Culhane, J. L., Harra, L. K., James, A. M., et al. 2007, SoPh, 243, 19
De Moortel, I., & Browning, P. 2015, RSPTA, 373, 20140269
De Moortel, I., & Pascoe, D. J. 2012, ApJ, 746, 31
Del Zanna, G., Dere, K. P., Young, P. R., & Landi, E. 2021, ApJ, 909, 38
Del Zanna, G., Dere, K. P., Young, P. R., Landi, E., & Mason, H. E. 2015,
    &A, 582, A56
Denskat, K. U., Beinroth, H. J., & Neubauer, F. M. 1983, JGZG, 54, 60
Denskat, K. U., & Neubauer, F. M. 1982, JGR, 87, 2215
Dere, K. P., Landi, E., Mason, H. E., Monsignori Fossi, B. C., & Young, P. R.
   1997, A&AS, 125, 149
Dmitruk, P., Matthaeus, W. H., Milano, L. J., et al. 2002, ApJ, 575, 571
Dmitruk, P., Milano, L. J., & Matthaeus, W. H. 2001, ApJ, 548, 482
Dobrowolny, M., Mangeney, A., & Veltri, P. 1980, PhRvL, 45, 144
Domingo, V., Fleck, B., & Poland, A. I. 1995, SoPh, 162, 1
Doschek, G. A., Mariska, J. T., Warren, H. P., et al. 2007, ApJL, 667, L109
Downs, C., Lionello, R., Mikić, Z., Linker, J. A., & Velli, M. 2016, ApJ,
   832, 180
Feldman, U. 1992, PhyS, 46, 202
Feldman, U. 1998, SSRv, 85, 227
Fujimoto, M., Shinohara, I., & Kojima, H. 2011, SSRv, 160, 123
Galtier, S., Nazarenko, S. V., Newell, A. C., & Pouquet, A. 2000, JPIPh,
  63, 447
Goldreich, P., & Sridhar, S. 1995, ApJ, 438, 763
Goldreich, P., & Sridhar, S. 1997, ApJ, 485, 680
Gombosi, T. I., Powell, K. G., De Zeeuw, D. L., et al. 2004, CSE, 6, 14
Gudiksen, B. V., & Nordlund, Å. 2005, ApJ, 618, 1031
Heinemann, M., & Olbert, S. 1980, JGR, 85, 1311
Henney, C. J., Toussaint, W. A., White, S. M., & Arge, C. N. 2012, SpWea,
   10, S02011
Hickmann, K. S., Godinez, H. C., Henney, C. J., & Arge, C. N. 2015, SoPh,
   290, 1105
Hoeksema, J. T., Liu, Y., Hayashi, K., et al. 2014, SoPh, 289, 3483
Hossain, M., Gray, P. C., Pontius, D. H., Matthaeus, W. H., & Oughton, S.
   1995, PhFl, 7, 2886
Hu, Y. Q., Li, X., & Habbal, S. R. 2003, JGRA, 108, 1378
Hughes, A. L. H., Bertello, L., Marble, A. R., et al. 2016, arXiv:1605.03500
Ionson, J. A. 1978, ApJ, 226, 650
Jin, M., Manchester, W. B., van der Holst, B., et al. 2013, ApJ, 773, 50
Kamio, S., Hara, H., Watanabe, T., Fredvik, T., & Hansteen, V. H. 2010, SoPh,
   266, 209
King, J. H., & Papitashvili, N. E. 2005, JGRA, 110, A02104
Klimchuk, J. A. 2006, SoPh, 234, 41
Kosugi, T., Matsuzaki, K., Sakao, T., et al. 2007, SoPh, 243, 3
Kuperus, M., Ionson, J. A., & Spicer, D. S. 1981, ARA&A, 19, 7
Laming, J. M. 2015, LRSP, 12, 2
Landi, E. 2007, ApJ, 663, 1363
```

Lemen, J. R., Title, A. M., Akin, D. J., et al. 2012, SoPh, 275, 17

```
Leroy, B. 1980, A&A, 91, 136
Lionello, R., Linker, J. A., & Mikić, Z. 2009, ApJ, 690, 902
Lithwick, Y., & Goldreich, P. 2003, ApJ, 582, 1220
Lithwick, Y., Goldreich, P., & Sridhar, S. 2007, ApJ, 655, 269
Magyar, N., Van Doorsselaere, T., & Goossens, M. 2017, NatSR, 7, 14820
Magyar, N., Van Doorsselaere, T., & Goossens, M. 2019, ApJ, 882, 50
Manchester, W. B., van der Holst, B., Tóth, G., & Gombosi, T. I. 2012, ApJ,
Mathioudakis, M., Jess, D. B., & Erdélyi, R. 2013, SSRv, 175, 1
Matsumoto, T., & Suzuki, T. K. 2012, ApJ, 749, 8
Matthaeus, W. H., Zank, G. P., Oughton, S., Mullan, D. J., & Dmitruk, P.
  1999, ApJL, 523, L93
Meng, X., van der Holst, B., Tóth, G., & Gombosi, T. I. 2015, MNRAS,
Ng, C. S., & Bhattacharjee, A. 1996, ApJ, 465, 845
Ofman, L. 2005a, AdSpR, 36, 1572
Ofman, L. 2005b, SSRv, 120, 67
Ofman, L., & Davila, J. M. 1998, JGR, 103, 23677
Oran, R., Landi, E., van der Holst, B., et al. 2015, ApJ, 806, 55
Oran, R., Landi, E., van der Holst, B., Sokolov, I. V., & Gombosi, T. I. 2017,
   ApJ, 845, 98
Oran, R., van der Holst, B., Landi, E., et al. 2013, ApJ, 778, 176
Osterbrock, D. E. 1961, ApJ, 134, 347
Pant, V., Magyar, N., Van Doorsselaere, T., & Morton, R. J. 2019, ApJ,
  881, 95
Parker, E. N. 1988, ApJ, 330, 474
Parnell, C. E., & De Moortel, I. 2012, RSPTA, 370, 3217
Perez, J. C., & Chandran, B. D. G. 2013, ApJ, 776, 124
Pesnell, W. D., Thompson, B. J., & Chamberlin, P. C. 2012, SoPh, 275, 3
Powell, K. G., Roe, P. L., Linde, T. J., Gombosi, T. I., & De Zeeuw, D. L.
  1999, JCoPh, 154, 284
Priest, E. R., & Schrijver, C. J. 1999, SoPh, 190, 1
Riley, P., Downs, C., Linker, J. A., et al. 2019, ApJL, 874, L15
Sachdeva, N., Tóth, G., Manchester, W. B., et al. 2021, ApJ, 923, 176
Sachdeva, N., van der Holst, B., Manchester, W. B., et al. 2019, ApJ, 887, 83
Scherrer, P. H., Schou, J., Bush, R. I., et al. 2012, SoPh, 275, 207
Schou, J., Scherrer, P. H., Bush, R. I., et al. 2012, SoPh, 275, 229
Seely, J. F., Feldman, U., Schühle, U., et al. 1997, ApJL, 484, L87
Shi, T., Landi, E., & Manchester, W. 2019, ApJ, 882, 154
Sokolov, I. V., van der Holst, B., Oran, R., et al. 2013, ApJ, 764, 23
Suresh, A., & Huynh, H. T. 1997, JCoPh, 136, 83
Suzuki, T. K., & Inutsuka, S.- 2005, ApJL, 632, L49, ichiro Suzuki, T. K., & Inutsuka, S.-I. 2006, JGRA, 111, A06101
Szente, J., Landi, E., Manchester, W. B., et al. 2019, ApJS, 242, 1
Szente, J., Landi, E., & van der Holst, B. 2022, ApJ, 926, 35
Taroyan, Y., & Erdélyi, R. 2009, SSRv, 149, 229
Tian, H., Li, G., Reeves, K. K., et al. 2014, ApJL, 797, L14
Tóth, G., Sokolov, I. V., Gombosi, T. I., et al. 2005, JGRA, 110, A12226
Tóth, G., van der Holst, B., & Huang, Z. 2011, ApJ, 732, 102
Tóth, G., van der Holst, B., Sokolov, I. V., et al. 2012, JCoPh, 231, 870
Tu, C.-Y., & Marsch, E. 1995, SSRv, 73, 1
Tu, C.-Y., Marsch, E., Wilhelm, K., & Curdt, W. 1998, ApJ, 503, 475
Tu, C.-Y., Pu, Z.-Y., & Wei, F.-S. 1984, JGR, 89, 9695
Turmon, M., Hoeksema, J. T., & Bobra, M. 2014, AAS Meeting, 224, 123.52
Usmanov, A. V., Goldstein, M. L., Besser, B. P., & Fritzer, J. M. 2000, JGR,
   105, 12675
van Ballegooijen, A. A., & Asgari-Targhi, M. 2018, JPhCS, 1100, 012027
van Ballegooijen, A. A., Asgari-Targhi, M., Cranmer, S. R., & DeLuca, E. E.
  2011, ApJ, 736, 3
van Ballegooijen, A. A., Asgari-Targhi, M., & Voss, A. 2017, ApJ, 849, 46
van der Holst, B., Huang, J., Sachdeva, N., et al. 2022, ApJ, 925, 146
van der Holst, B., Manchester, W. B., Frazin, R. A., et al. 2010, ApJ, 725, 1373
van der Holst, B., Manchester, W. B., Klein, K. G., & Kasper, J. C. 2019,
   ApJL, 872, L18
van der Holst, B., Sokolov, I. V., Meng, X., et al. 2014, ApJ, 782, 81
Van Doorsselaere, T., Srivastava, A. K., Antolin, P., et al. 2020, SSRv,
Velli, M., Grappin, R., & Mangeney, A. 1989, PhRvL, 63, 1807
Velli, M., Pucci, F., Rappazzo, F., & Tenerani, A. 2015, RSPTA, 373, 20140262
Verdini, A., & Velli, M. 2007, ApJ, 662, 669
Wilhelm, K., Curdt, W., Marsch, E., et al. 1995, SoPh, 162, 189
Worden, J., & Harvey, J. 2000, SoPh, 195, 247
Zank, G. P., Dosch, A., Hunana, P., et al. 2012, ApJ, 745, 35
Zank, G. P., Matthaeus, W. H., & Smith, C. W. 1996, JGR, 101, 17093
Zhou, Y., & Matthaeus, W. H. 1990, JGR, 95, 14881
Zirker, J. B. 1993, SoPh, 148, 43
```